

Inhibiting recombination to improve the performance of plasma-based CO₂ conversion

Kaiyi Wang^{a,1}, Sara Ceulemans^{b,1}, Hao Zhang^{a,c,*}, Ivan Tsonev^b, Yilin Zhang^a, Yanhui Long^a, Mengxiang Fang^c, Xiaodong Li^a, Jianhua Yan^a, Annemie Bogaerts^{b,*}

^a. State Key Laboratory of Clean Energy Utilization, Zhejiang University, Hangzhou 310027, China

^b. Research group PLASMANT, Department of Chemistry, University of Antwerp, Wilrijk-Antwerp BE-2610, Belgium

^c. Zhejiang University Qingshanhu Energy Research Center, Hangzhou 311305, China

¹. These authors contributed equally to this work.

* Corresponding authors:

zhang_hao@zju.edu.cn (H. Zhang);

annemie.bogaerts@uantwerpen.be (A. Bogaerts)

Supplemental Information is available:

Additional information on the experimental setup, model description, and simulation results.

Abstract

Warm plasma offers a promising route for CO₂ splitting into valuable CO, yet recombination reactions of CO with oxygen, forming again CO₂, have recently emerged as critical limitation. This study combines experiments and fluid dynamics + chemical kinetics modelling to comprehensively analyse the recombination reactions upon CO₂ splitting in an atmospheric plasmatron. We introduce an innovative *in-situ* gas sampling technique, enabling 2D spatial mapping of gas product compositions and temperatures, experimentally confirming for the first time the substantial limiting effect of CO recombination reactions in the afterglow region. Our results show that the CO mole fraction at a 5 L/min flow rate drops significantly from 11.9% at a vertical distance of $z = 20$ mm in the afterglow region to 8.6% at $z = 40$ mm. We constructed a comprehensive 2D model that allows for spatial reaction rates analysis incorporating crucial reactions, and we validated it to kinetically elucidate this phenomenon. $CO_2 + M \rightleftharpoons O + CO + M$ and $CO_2 + O \rightleftharpoons CO + O_2$ are the dominant reactions, with the forward reactions prevailing in the plasma region and the backward reactions becoming prominent in the afterglow region. These results allow us to propose an afterglow quenching strategy for performance enhancement, which is further demonstrated through a meticulously developed plasmatron reactor with two-stage cooling. Our approach substantially increases the CO₂ conversion (e.g., from 6.6% to 19.5% at 3 L/min flow rate) and energy efficiency (from 13.5% to 28.5%, again at 3 L/min) and significantly shortens the startup time (from ~150 s to 25 s). Our study underscores the critical role of inhibiting recombination reactions in plasma-based CO₂ conversion and offers new avenues for performance enhancement.

Keywords: plasma-based CO₂ splitting; recombination reactions; *in-situ* gas sampling; fluid dynamics modeling; kinetics modeling; afterglow quenching

1. Introduction

The atmospheric concentration of carbon dioxide (CO_2) has surged to an unprecedented level of 415 ppm, primarily driven by anthropogenic emissions [1]. Addressing this global challenge necessitates innovative approaches to convert and utilize CO_2 as a valuable feedstock for producing added-value products, including carbon monoxide (CO), methanol, methane, formaldehyde, dimethyl ether, etc [2-5]. Particular emphasis has been placed on CO_2 splitting to produce CO, since CO is one of the most important C_1 feedstock for synthesizing a range of fuels and chemicals [6-8].

However, the thermodynamic stability of CO_2 molecules presents a formidable obstacle, demanding substantial energy inputs to affect its splitting. For instance, a high temperature of up to 3500 K is required to achieve a thermal CO_2 conversion of 60–80% [9]. A diverse array of CO_2 splitting routes has been explored, encompassing electrochemical, thermochemical, photochemical, biochemical, and catalytic methods [9-12]. However, each of these routes presents distinct challenges that impede their widespread adoption, including low conversion (e.g., <1% for the thermochemical method [13]), restricted productivity (e.g., <20 mg/(L·h) for the biochemical method [14]), the absence of efficient and cost-effective catalysts, and / or often sluggish reaction kinetics [13-16].

In this context, atmospheric warm plasma processes have risen to the forefront as a promising avenue for CO_2 conversion [9,17]. Plasma operates by applying electrical energy to generate a cocktail of reactive species (electrons, ions, radicals, excited species) that can initiate and further propagate reactions [18-21]. This distinctive behaviour makes it possible to facilitate thermodynamically unfavourable CO_2 conversion at atmospheric pressure and reduced energy costs. Moreover, plasma processes ensure rapid start-up, high reaction rates, compactness, ease of installation, and flexibility. These attributes enable the direct utilization of electricity generated from intermittent renewable sources, such as solar and wind power, offering a flexible solution for peak shaving and grid stabilization [9].

However, despite significant efforts, various plasma types, including dielectric barrier discharge (DBD), microwave (MW), gliding arc (GA), and radio frequency (RF) discharge, still face challenges, such as low energy efficiency (e.g., DBD, <10%) or limited CO_2 conversion (e.g., MW, GA, RF, <20% [9,22,23]). Strategies to enhance gas treatment by plasma and promote the efficient vibration-induced dissociation have yielded improvements in so-called warm plasmas, like MW and GA [24-27], although the conversion in practice is dominated by thermal chemistry, when operating at atmospheric pressure [24].

Nevertheless, recent studies suggest that recombination reactions in the afterglow region, especially in the case of widely explored warm plasma systems like MW, GA, and RF, which feature relatively high gas temperatures of 3000 K and above, may be critical limiting factors [24,28-32]. In certain scenarios, the

efficiency constraints may primarily stem from recombination reactions in the post-plasma region, rather than production limitations within the plasma itself [33].

A chemical kinetics modelling study of MW plasma indicated that at high energy inputs, the CO₂ conversion can plummet from a theoretically high 100% to around 20-25%, primarily due to recombination reactions in the afterglow region [28]. Moreover, recent experimental research involving MW plasma, supported by modelling, demonstrated that the introduction of a converging-diverging nozzle in the post-plasma section resulted in a remarkable 21% relative increase in energy efficiency, likely attributed to the quenching effect on the afterglow, which curbs recombination reactions [29]. A similar behaviour was reported in a modelling study [30], explaining spectacular performance improvements observed experimentally [34]. Indeed, it was computationally demonstrated that introducing a nozzle in the plasma effluent induces fast gas quenching, due to both enhanced convective and conductive cooling, thereby significantly suppressing the recombination reactions [30]. Furthermore, experimental endeavours in the realm of microwave plasmas have included the utilization of a water-cooled quenching rod or nozzle [35,36], cooling channels with reverse vortex [37], and membrane separation of oxygen [38,39].

Nevertheless, the significance of reverse reactions in plasma-assisted CO₂ splitting has not been directly validated through experiments. This can potentially be probed by tracking the spatial evolution of the CO concentration along the flow rate direction. However, given the high reactivity of gas products and the elevated temperatures in the reaction area, accurately *in-situ* detecting species concentrations poses a significant challenge, due to secondary reactions that proceed during the sampling process (even for stable species), which is normally neglected in current methods [40]. A new sampling method, allowing for *in-situ* detection of the spatial distribution, and a deeper understanding of the competition between splitting and recombination reactions are essential for advancing our knowledge of plasma-based CO₂ conversion.

In this work, we employed an atmospheric pressure plasmatron reactor for CO₂ splitting. We developed an *in-situ* gas sampling setup to image the 2D spatial distribution of the gas product composition and temperature in the afterglow region. To understand the underlying mechanisms, we constructed a comprehensive 2D axisymmetric fluid dynamics model, incorporating crucial chemical reactions, which we validated against the 2D experimental data, allowing us to elucidate the spatial competition dynamics between CO₂ splitting and recombination reactions. Last but not least, to experimentally validate the proposed afterglow quenching strategy aimed at optimizing the performance, we designed and evaluated a plasmatron reactor equipped with a two-stage cooling system. This innovative setup allowed us to examine the practical implications of our proposed approach and its impact on the CO₂ conversion performance.

2. Methods

2.1 Experiment

A schematic of the homemade atmospheric plasmatron reactor is presented in Fig. 1, while the entire experimental system is schematically illustrated in Fig. S1 in Section S1 of the supplementary information (SI). The homemade plasma reactor consists of a cylindrical inner anode and a convergent nozzle-shaped outer cathode (grounded), between which a rotating gliding arc plasmatron can be formed under the influence of a strong electric field. The reactor configuration has been described previously in detail [25,41], and we applied only minor modifications in this work. The feed gas CO₂ (purity 99.99%), controlled by a mass flow controller (MFC, YJ-700C) at a flow rate of 5 or 7 L/min, was injected into the reactor from the bottom through three tangential inlets, to form a swirling flow inside the reactor. After being initiated at the narrowest gap (1 mm) between the electrodes, the arc is pushed downstream and then extends from the convergent exit nozzle to form a 3D plasmatron outside of the electrode region. A customized 10 kV DC power supply (TLP2040, Teslaman) was employed to power the discharge with a 40 k Ω resistance connected in series in the circuit to stabilize the discharge current. The discharge voltage and current were measured using a high-precision oscilloscope (Tektronix MDO3024, 200 MHz bandwidth) equipped with a high-voltage probe (Tektronix P6015A) and a current probe (Magnetlab CT-E0.5-BNC).

We designed a sampling chamber (50 × 55 × 230 mm cuboid, stainless steel with a quartz window) with 11 vertically distributed holes in the wall for inserting the sampling set, which was assembled downstream the electrode, as schematically shown in Fig. 1. The *in-situ* sampling chamber consists of an outer alumina ceramic tube (inner / outer diameter = 1 mm / 2 mm) that splits in the middle with a gap of 0.4 mm, and an inner stainless-steel needle (inner / outer diameter = 0.3 mm / 0.6 mm) with the tip placed near the gap of the ceramic tube. During the sampling, carrier gas (N₂) with a flow rate of 1 L/min was injected into the needle, forming a fast flow speed of around 235 m/s at the tip that can extract around 0.3 L/min reactive gas from the chamber into the ceramic tube. In this way, the sampled gas can be *in-situ* diluted by a factor of ~4 and cooled down to an estimate of 400-600 K (see Section S1 in SI for detailed calculation), thereby “freezing” the chemical composition of the sampled gases by largely inhibiting the secondary reactions during sampling.

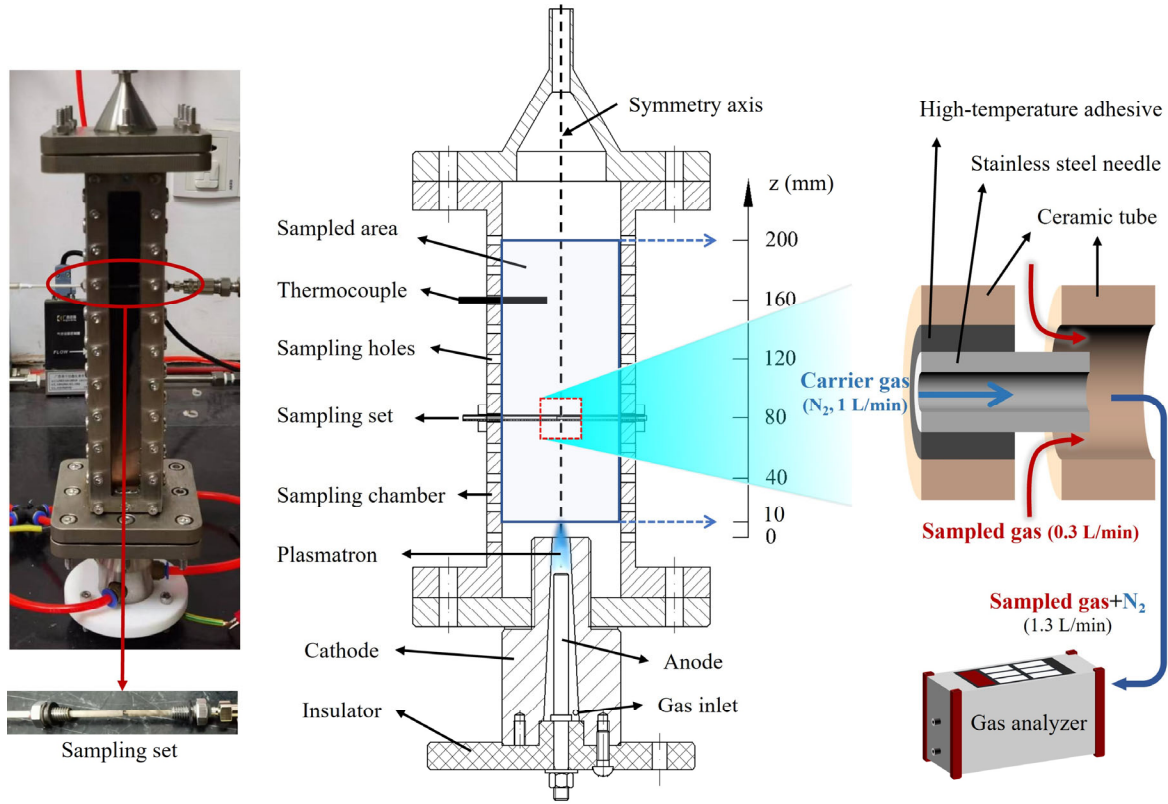


Fig. 1. Picture (left) and schematic (middle) of the plasmatron reactor and the sampling chamber, and enlarged view (right) of the *in-situ* sampling set.

The effluent of the ceramic tube, containing the sampled gas ($\text{CO}_2 + \text{CO} + \text{O}_2$) and carrier gas (N_2), was then analysed by a flue gas analyser (MRU vario plus) equipped with non-dispersive infrared (NDIR) sensors for CO_2 and CO detection and an electrochemical sensor for O_2 detection. Each experiment was repeated three times and the averaged values were collected. The CO concentration in the sampled gas (C_{CO}^s) and the CO_2 conversion (X_{CO_2}) were then calculated based on the carbon and oxygen elemental balance, as defined in Eq. (1) and Eq. (2) [23].

$$C_{\text{CO}}^s(\%) = \frac{Q_{\text{CO}}^s(\text{L/min})}{Q_{\text{tot}}^s(\text{L/min})} = \frac{C_{\text{CO}}^r(\%) \cdot Q_{\text{tot}}^r(\text{L/min})}{[C_{\text{CO}_2}^r(\%) + C_{\text{CO}}^r(\%) + C_{\text{O}_2}^r(\%)] \cdot Q_{\text{tot}}^r(\text{L/min})}$$

$$= \frac{C_{\text{CO}}^r(\%)}{C_{\text{CO}_2}^r(\%) + C_{\text{CO}}^r(\%) + C_{\text{O}_2}^r(\%)} \quad (1)$$

$$X_{\text{CO}_2}(\%) = \frac{C_{\text{CO}}^r(\%)}{C_{\text{CO}_2}^r(\%) + C_{\text{CO}}^r(\%)} \quad (2)$$

where Q_{tot}^s and Q_{tot}^r is the total gas flow rate of the sampled gas and the effluent of the ceramic tube, respectively; Q_{CO}^s is the flow rate of CO in the sampled gas; $C_{CO_2}^r$, C_{CO}^r and $C_{O_2}^r$ are the concentrations of CO₂, CO and O₂, respectively, in the effluent of the ceramic tube. The selectivity of CO was assumed to be 100%, in line with nearly all reported works on plasma-assisted CO₂ splitting [9]. Indeed, the mean electron energy of the plasmatron system (~1-1.5 eV) is considered too low to produce remarkable coke from CO₂. Also, we did not observe any solid residues on the electrode surface nor in the gas-phase products during long-term operation. Moreover, since there is no H element in our reaction system, it is not possible to generate hydrocarbons.

The energy efficiency (η) was defined as [9,25]:

$$\eta(\%) = \frac{X_{CO_2}(\%) \times Q_{in}(mol/min) \times \Delta H(kJ/mol) \times 1000(J/kJ)}{Discharge\ power(W) \times 60(s/min)} \quad (3)$$

where Q_{in} is the inlet total flow rate; ΔH is the standard reaction enthalpy for the pure CO₂ decomposition reaction ($\Delta H = 280\ kJ/mol$) [9,25].

The specific energy input (SEI) was defined as:

$$SEI(eV/molecule) = \frac{Discharge\ power(W) \times 60(s/min) \times V_m(L/mol)}{Q_{tot}^{in}(L/min) \times 1.60 \times 10^{-19}(J/eV) \times N_A(molecule/mol)} \quad (4)$$

where Q_{tot}^{in} is the inlet flow rate; V_m is the molar volume of gas (22.41 L/mol at 273 K and 1 atm); N_A is the Avogadro's constant ($6.022 \times 10^{23}\ molecule/mol$).

The gas products at different locations can be sampled by moving the sampling set vertically and horizontally in the axial cross section. The sampled area spans from a vertical distance of $z = 10\ mm$ to $z = 200\ mm$ in the afterglow region ($z = 0\ mm$ is the position of the electrode exit), as shown in Fig. 1. To avoid any significant influence of the sampling set on the arc discharge, the gas products were only sampled and measured for $z > 20\ mm$. A 2D spatial distribution map of the gas product compositions in the range of $z = 20-200\ mm$ was then derived by means of a spline method for two-dimensional interpolation, based on the measured results at the distributed points.

The gas temperature is of vital importance in governing the reactions in the afterglow area, and was therefore measured as well. The 2D temperature profile at $z = 10-200\ mm$ was derived in a similar way as described above, by replacing the gas sampling set with a thermocouple (S type).

2.2 Model description

2.2.1 Geometry and gas flow

To reduce the geometrical complexities, we slightly adapted the modelled reactor, shown in Fig. 2, compared to the experimental reactor. The primary change involves approximating the rectangular exhaust of the experiments with a cylinder of the same cross-sectional area and volume in the model. This allows us to use a 2D axisymmetric model instead of a 3D model, significantly reducing the simulation time. Some parts of the reactor are also cut off in the model, including the bottom part. This is justified because the arc is connected to the horizontal top edge of the anode, and therefore the start of the reactor is less important. Consequently, the three tangential inlets are replaced by one ring-shaped inlet, corresponding to one surface in the 2D axisymmetric model, as shown in Fig. 2b. The gas velocity at this 2D axisymmetric surface inlet (a swirl flow) is obtained from a 3D model of the reactor that is solved for the gas flow only. This approach is justified because, at the inlet, the gas has not yet reached the plasma, and its temperature and properties are thus not affected by the plasma and remain unchanged. Therefore, the inlet velocity will only be influenced by the geometry, for the gas at room temperature, and other physics do not need to be included for accurate results. In addition, because there are three tangential inlets in the experimental setup, each creating a swirling flow with a 120° rotation relative to each other, the gas flow at the height of the 2D axisymmetric model inlet, i.e., -15 mm, is a combination of these three flows and has an approximately 2D axisymmetric velocity profile in the xy-plane. The explanation of how the inlet velocity is obtained and implemented in the 2D axisymmetric model can be found in Section S2.1 and Fig. S2 in SI.

The gas flow in the model is calculated using the Navier-Stokes equations for weakly compressible flow, i.e., the gas density only depends on the temperature but not on the pressure, the gas is considered an ideal gas and a laminar flow is assumed. We performed some initial tests with a model with turbulent flow, but we decided to continue with a laminar flow model. Indeed, due to the large size of the model, including turbulence would make the calculation times excessively long. Furthermore, modelling turbulence resulted in calculation instabilities, and our initial tests with a turbulent flow model also did not result in significantly better comparison with the experiments, because even when adding turbulence, not all the effects that influence the gas flow experimentally, such as attachment or detachment of the arc, are included. To verify whether a laminar flow model would be sufficient, we calculated the Re number based on Ref. [42], at the inlet, in the plasma and in the exhaust, and we obtained values below 1200 at all positions and conditions investigated. Because this is below the critical Re number of 2000, mentioned in Ref. [43], it justifies the use of a laminar flow. The choice of laminar flow simplifies the model and provides reasonable results without introducing calculation instabilities associated with turbulence. Crucially, our model accounts for the significant effects of turbulence, such as cooling and mixing, either within the model itself or during

results analysis. In addition, as the reactor's diameter decreases in the axial flow direction, the axial gas velocity increases, leading to a reduction in gas swirl, which might make the flow more laminar. More information on the gas flow simulation and the used equations and boundary conditions can be found in Section S2.1 in SI.

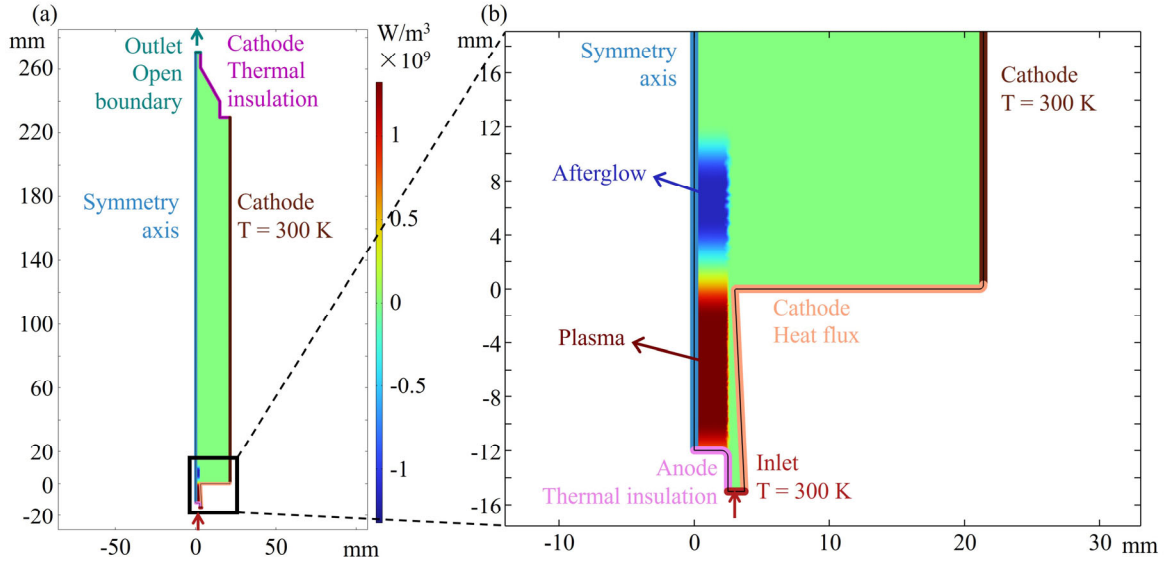


Fig. 2. (a) Schematic of the reactor and exhaust geometry in the model, and (b) enlarged view of the reactor indicated with a black frame in (a). The boundary conditions (set temperature, heat flux or thermal insulation) are given for each boundary. The colour scale represents the applied heat source (to mimic the plasma power density), with negative values representing cooling after the plasma.

2.2.2 Heat transfer

Heat transfer in the model is calculated by the heat balance equation, which is given and explained in Section S2.2 in SI. A heat source is used to mimic the plasma, representing the Joule heating from the plasma. This simplification allows for a computationally tractable model, aligning with our primary focus on temperature and CO_2 chemistry rather than the electrical properties of the plasma. This approach has already been successfully used in previous research for a rotating gliding arc reactor [44]. The heat source in this model has a cylindrical shape with a length of 12 mm from the anode up to the end of the reactor and the start of the exhaust, and has a radius of 2.5 mm. The power distributed over the cylinder is taken from the experiments: 303 W and 320 W for 5 L/min and 7 L/min, respectively. The shape and power density distribution of the heat source in W/m^3 for 5 L/min are shown in Fig. 2b, denoted as “plasma”. With these power values, temperatures up to 3200-3350 K are reached, consistent with previous findings, indicating temperatures around 3000 K for gliding arc reactors in general [45-49].

Adjacent to the heat source, a heat sink is added to the model, positioned approximately 3 mm after the end of the heat source. It also has a cylindrical shape with the same radius and a length of 7 mm. Its power increases with increasing flow rate (see explanation below), with values set at 160 W and 185 W for 5 L/min and 7 L/min, respectively. The location, shape and power density distribution of the heat sink for 5 L/min are indicated as the afterglow in Fig. 2b. This heat sink accounts for cooling effects that are not included in the model. Specifically, turbulent heat transfer is absent because we assume a laminar flow. In reality, the complex movement of the arc, including attachment, detachment and reattachment, disturbs the flow, which would lead to a turbulent flow. However, because it is too complicated and computationally expensive to take the arc movement and turbulence into account in our model, we include the turbulent cooling effect by adding a heat sink, which, like turbulence, increases in cooling power with increasing flow rate. A more detailed justification for adding this heat sink, including references, can be found in Section S2.2 in SI.

We did not include radiative heat losses in our model. Indeed, we can estimate the radiative energy loss, based on [50]. The maximum temperature obtained in our simulations is 3323 K, which corresponds to a net emission coefficient between 1 and 10 W cm⁻³ sr⁻¹, approximately 5 W cm⁻³ sr⁻¹, for a pressure of 1 bar and an isothermal plasma cylinder radius of 1 mm. To convert this to a heat loss in W cm⁻³, we multiply this by the solid angle of a complete sphere, i.e., 4 π sr. This yields a radiative heat loss of 62.8 W cm⁻³. In our simulations, the bulk power density of the heat source is 1326 W cm⁻³ and 1401 W cm⁻³, for 5 L/min and 7 L/min, respectively, and thus, the radiative heat loss would be only 4.7% or 4.5% of this power density. In reality, the radiative heat loss will be even lower, because the plasma radius applied in our model is 2.5 mm, and according to [50], the net emission coefficient decreases with increasing plasma radius. Hence, for the plasma, we can estimate the radiative heat loss to be less than 5% of the power density of the heat source at a maximum plasma temperature of 3323 K. In the afterglow, the cooling effect of radiative heat loss will be even smaller, and can also be neglected.

To consider the heat loss at the reactor walls, we use a heat flux for the reactor walls and the start of the exhaust (in orange in Fig. 2), with the temperature of the cylinder side set at 300 K (in brown in Fig. 2). The top part of the exhaust, at the outlet, and the anode are thermally insulated, while the gas enters the reactor through the inlet at a temperature of 300 K. These boundary conditions are also shown in Fig. 2 and are explained in more detail, together with the equations, in Section S2.2 in SI.

2.2.3 Chemistry

The chemistry set included in the model is obtained from GRI-Mech 3.0 [51] and Ref. [52]. The model includes five species, i.e., CO₂, CO, O₂, O and C, and six equilibrium reactions, which are presented, together with their forward rate coefficients, in Table 1.

Table 1. Reactions included in the model with their forward reaction rate coefficients k_f . The reverse rate coefficients are calculated based on the principle of detailed balancing. M stands for any of the five species included in the model. The units of the forward rate coefficients are $\text{cm}^3 \text{mol}^{-1} \text{s}^{-1}$ for two-body reactions and $\text{cm}^6 \text{mol}^{-2} \text{s}^{-1}$ for three-body reactions.

Reaction		Forward rate coefficient
1	$O + CO + M \rightleftharpoons CO_2 + M$	$c_{eff} = 3.5c_{CO_2} + 1.5c_{CO} + 6c_{O_2} + c_O + c_C$ $k_o = 6.02 \times 10^{14} \times \exp(-3000[\text{cal/mol}]/RT)$ $k_{inf} = 1.80 \times 10^{10} \times \exp(-2385[\text{cal/mol}]/RT)$ $k_f = k_{inf}/(1 + k_{inf}/(k_o c_{eff}))$
2	$CO + O_2 \rightleftharpoons CO_2 + O$	$k_f = 2.50 \times 10^{12} \times \exp(-47800[\text{cal/mol}]/RT)$
3	$C + O_2 \rightleftharpoons O + CO$	$k_f = 5.80 \times 10^{13} \times \exp(-576[\text{cal/mol}]/RT)$
4	$2O + M \rightleftharpoons O_2 + M$	$c_{eff} = 3.6c_{CO_2} + 1.75c_{CO} + c_{O_2} + c_O + c_C$ $k_f = 1.20 \times 10^{17}/T \times c_{eff}$
5	$CO_2 + C \rightleftharpoons 2CO$	$k_f = 1.0 \times 10^{-15} \times N_A$
6	$C + O + M \rightleftharpoons CO + M$	$c_{eff} = c_{CO_2} + c_{CO} + c_{O_2} + c_O + c_C$ $k_f = 2.14 \times 10^{-29} \times (T/300)^{-3.08} \times \exp(-2114/T) \times N_A^2 \times c_{eff}$

The reverse rate coefficients are obtained through detailed balancing, by calculating the ratio of the forward rate coefficient and the equilibrium constant. The latter is determined from the enthalpy and entropy of the reaction. Since we concentrate predominantly on CO_2 splitting and its backward recombination, we limited the chemistry set to only thermal chemistry, including two CO_2 splitting/recombination reactions, to simplify the model. Indeed, chemical kinetics modelling has revealed that CO_2 conversion is mainly thermal at the typical plasma gas temperatures around 3000-4000 K under study here, even though in these simulations the pressure was lower and the specific energy input higher [28], so the approximation of only considering thermal chemistry is even more valid in the present work. In the following sections, we will refer to the CO_2 splitting reaction as the forward reaction and to recombination as the backward reaction, in contrast to the reaction equations in the table. More information on the chemistry and the transport of these species through the reactor is given in Section S2.3 in SI.

The Navier-Stokes equations, heat balance equation and the equation for chemical transport of each species (see Section S2.1-S2.3 in SI) are solved self-consistently in a fully coupled manner. The transport properties (heat capacity, viscosity, thermal conductivity and density) of the gas are a function of the gas composition within each point of the reactor, meaning that chemical equilibrium is not a priori assumed. The equations for these mixture-dependent gas properties are given in Section S2.3 in SI. We used a time-dependent solver and chose a calculated time exceeding 30 seconds. This allows for the dispersion of species concentrations throughout the reactor and minimizing further significant variations. In addition, we added the condition that the mass fraction of atomic carbon C cannot decrease below 10^{-13} for 5 L/min, or below 10^{-8} for 7 L/min.

This increases the stability of the model, with values sufficiently low to have a negligible impact on the results.

3. Results and Discussion

In this section, we begin by discussing the measured and simulated spatial distributions of gas temperature in Section 3.1 and CO mole fraction in Section 3.2. Subsequently, Section 3.3 delves into the analysis of the underlying reactions, shedding light on the spatial significance of dissociation and recombination reactions. Finally, in Section 3.4, we demonstrate the proposed afterglow quenching strategy through the use of a specially developed plasmatron reactor equipped with a cooling system. We were unable to measure the temperature and CO mole fraction at $z = 0$ mm, because the thermocouple and sampling tube experienced discharge with the inner electrode. In our future work, we will try to employ quartz probe-sampled molecular beam mass spectrometry (MBMS) to measure the CO mole fraction at $z = 0$ mm.

3.1 Gas temperature

The measured and calculated temperatures of the afterglow area for two different gas flow rates are presented in Fig. 3, illustrating both the spatial distribution (Figs. 3a-d) and the values along the central axis (Fig. 3e). At small radial distances, i.e., close to the symmetry axis, the calculated temperature is in general too high compared to the experimental temperature. For example, when calculating the average difference between the calculated and experimental temperature along the symmetry axis, at $r = 0$ mm, we find that the calculated temperature is on average 85% and 106% higher than the experimental temperature, for 5 L/min and 7 L/min, respectively. In contrast, at larger radial distances, i.e., closer to the walls, the calculated temperature is too low compared to the experimental values (Figs. 3a-d). For example, for $r = 10$ mm, the calculated temperature is on average 26% and 37% lower than the experimental values, for 5 L/min and 7 L/min, respectively. The calculated temperature is in general too high close to the symmetry axis and too low away from the axis (Figs. 3a-d). This might be due to the mixing between the cold gas flow surrounding the plasma and the hot core region of the discharge that is caused by the turbulent effect (not yet considered in our model), as mentioned above. The heat sink, included to take this cooling effect into account, will only remove the heat from the model instead of spreading the heat radially over the exhaust through turbulent mixing. Nevertheless, the temperature drop along the central axis, and the nearly constant temperature away from the central axis, can be qualitatively captured by the simulations. Since we will mainly focus on the region close to the central axis to explain the experimental observations, the heat sink considered in our model provides an adequate solution to account for the turbulent cooling and mixing effects on this axis. Note that the deviation between experiments and calculations may also partly be attributed to the uncertainty in the measurements caused by the effect of the sampling set on the local gas.

We estimated the total heat transfer between the sampling set and the afterglow to be about 3.79 W, which is only approximately 1.2% of the discharge power. We believe that this could be ignored. In other words, the cooling effect will not take place through the tubes, but at the point where the tubes take in part of the sampled gas.

Figs. 3a-d also show an important property of the gas flow. Away from the central axis, at higher radial distances, the gas temperature becomes somewhat higher at higher axial positions, compared to the gas temperature at lower axial position for the same radial distance. Indeed, the temperature is radially not uniform both in the model and the experiment, owing to a large recirculation zone forming in the exhaust of the reactor. More specifically, at a radial distance equal to 10 mm, the calculated temperature increases from 381 K to 444 K for 5 L/min, and from 342 K to 362 K for 7 L/min, upon rising axial position in the exhaust from 40 mm to 200 mm. As clearly seen from the flow velocity maps presented in Fig. S3 of Section S3.1 in SI, part of the gas recirculates back because of the decreasing reactor diameter at the end, and warm gas coming from close to the symmetry axis is divided over the region further away from the axis, thus spreading out the heat there. The comparison of the post-plasma temperature profiles between the experiment and the model shows a clear difference. The reason for this is the underestimated mixing by our model. We also performed simulations with a turbulent model, but they did not yield significantly better results and led to much longer calculation time. The nature of the turbulence in the post-plasma region arises from both continuous attachment and detachment of the arc and complicated interactions between the swirling flow and the very hot plasma. Despite the fact that we did not capture accurately the mixing post-plasma, we designed the model such that it can shed light into the mechanisms driving CO₂ conversion.

A significant drop in the temperature along the central axis (z) can be clearly observed for all cases, especially from the starting measuring point of $z = 10$ mm to $z = 40$ mm. For instance, at a flow rate of 5 L/min, the measured gas temperature decreases dramatically from 1288 K at $z = 10$ mm to 712 K at $z = 40$ mm (average temperature gradient of 19 K/mm), and then declines slowly to 474 K at $z = 200$ mm (average temperature gradient of 1.5 K/mm), as plotted in Fig. 3e. We can make a similar calculation of the temperature gradient in the model, which we can further convert to a cooling rate, because the model also calculates the velocity. The temperature gradients in the model are 21 K/mm between $z = 10$ mm and $z = 40$ mm (i.e., from 2129 K to 1505 K), and 4.4 K/mm going to $z = 200$ mm (at a temperature of 807 K). Our model calculates an average velocity on the symmetry axis of 22795 mm/s (nearly 23 m/s) from $z = 10$ mm to $z = 40$ mm, and of 13382 mm/s (ca. 13 m/s) from $z = 40$ mm to $z = 200$ mm. By multiplying this average velocity with the temperature gradients, we can estimate the cooling rate to be equal to 4.74×10^5 K/s between 10 and 40 mm, and 5.84×10^4 K/s between 40 and 200 mm. In Ref. [47], it is pointed out that a cooling rate of about 10^7 K/s or higher is required to retain the dissociation products and avoid

recombination reactions. From our calculated values, it is clear that, without any quenching, these cooling rates are not achieved. The model clearly overestimates the absolute values of the temperature, but it can qualitatively predict the drop in temperature. Importantly, while the calculated temperature is around 3000 K in the plasma, and probably also in the experiments (although it is not measured, but this value is generally accepted to be typical for warm plasmas), it drops to below 2000 K, at 15.89 mm and 19.32 mm for 5 L/min and 7 L/min, respectively. This is important, because it indicates that the model covers the temperature range between 3000 and 2000 K, in which both CO₂ splitting and recombination take place. Indeed, below 2000 K, the rates of these reactions are significantly reduced, and the gas composition will change less. This will be discussed in more detail in Section 3.3 below. However, even though the composition does not vary a lot anymore at temperatures lower than 2000 K, this does not mean that quenching further down the exhaust, at higher axial positions, will have no effect. Indeed, due to the recirculation shown in Fig. S3, the gas closer to the walls will flow down to lower axial heights and quench the gas that still has a temperature higher than 2000 K. Altogether, the fact that the calculated temperature is higher than the measured values is not critical to explain the mechanisms, because most important is that the calculated temperature has dropped to below 2000 K.

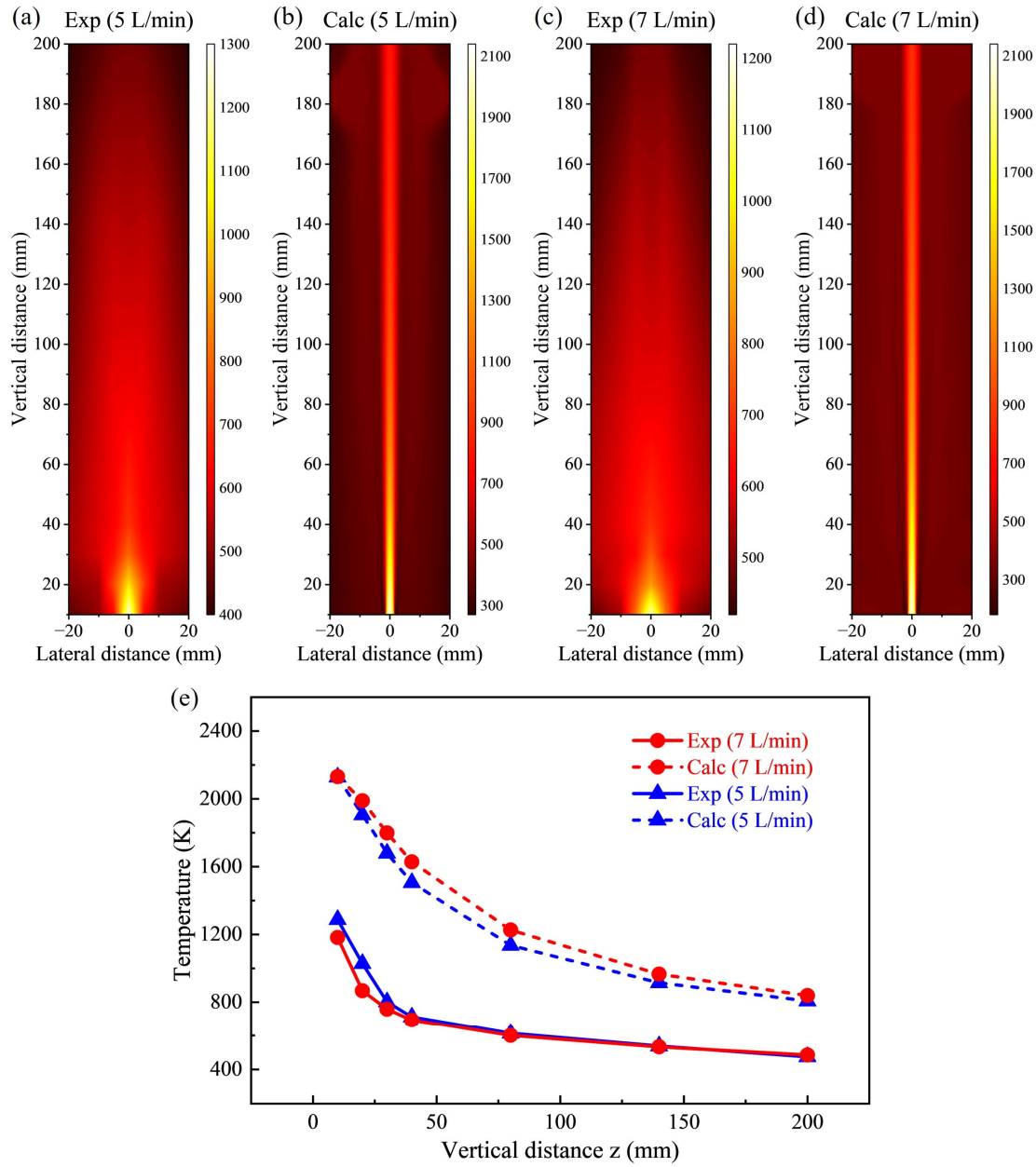


Fig. 3. Comparison of the experimental and calculated temperature profiles (in K) for 5 L/min and 7 L/min. (a-d): 2D distribution maps; (e): 1D plots at the central axis. (Discharge power: 303 W at 5 L/min and 320 W at 7 L/min)

3.2 CO mole fraction

The profiles of measured and calculated CO mole fraction, as well as those along the central axis at 5 or 7 L/min, are presented in Fig. 4. The experimental CO mole fractions exhibit torch-like spatial distribution

profiles. Again, we see an overestimate in the model prediction for CO mole fractions close to the central axis, but the difference between model and experiments away from the axis depends on the flow rate: at 5 L/min the experimental and calculated values lie very close to each other, and at 7 L/min the calculated CO mole fraction is too low. The explanation for this is given in the next paragraph. Nevertheless, similar to the temperature profiles, the decreasing trend along the central axis, and the nearly constant trend away from the central axis align between the experiments and simulations. As seen from Figs. 4a-d, a modest elevation in CO mole fraction can be discerned at specific vertical distances away from the central axis, which is more evident in the experimental measurements, although it is also present (but less clear) in the simulation results. This phenomenon can likely be attributed to the recirculation of CO, which follows the downward flow direction within the region situated between the reactor's central axis and its wall. This recirculation pattern is visually represented by the calculated flow direction arrows presented in Fig. S3 in SI. In this way, CO is spread out inside the exhaust. The evolution of the recirculation zone could be observed over time throughout the entire 30 seconds of the simulation. The increase in CO molar fraction after 160 mm is likely a result of an artefact of the sampling method. It could be due to factors such as spatial resolution, flow field effects, or other experimental uncertainties.

The observed higher CO mole fraction along the central axis in the simulations is likely attributed to the overestimate in the gas temperature, as discussed above. The difference away from the symmetry axis can be explained by a combination of a difference in temperature and the presence of turbulent mixing, which causes enhanced diffusion, spreading the CO away from the central axis in the experiments. The higher temperature in the model at lower radial positions, close to the symmetry axis, will lead to a higher CO mole fraction, which, due to the higher concentration gradient, can spread out faster through diffusion to higher radial positions. On the other hand, the temperature closer to the reactor walls is higher in the experiments and this will produce a higher CO mole fraction through chemical reactions. In addition, as mentioned before, turbulent mixing is present in the experiments, which results in a higher CO mole fraction closer to the walls, especially for higher flow rates, in the experiments compared to the model, where this turbulent mixing is not taken into account. The combination of these effects results in a similar experimental and calculated CO mole fraction for 5 L/min and a higher experimental CO mole fraction for 7 L/min. Furthermore, the sampling set in the measurement could also underestimate the CO mole fraction due to the variations introduced in the flow field, as reported in the flame sampling probe [53].

As seen from Fig. 4e, the measured CO mole fraction at the central axis drops significantly from $z = 20$ mm to $z = 40$ mm, i.e., from 11.9% to 8.6% and from 10.5% to 7.5% for 5 and 7 L/min, respectively, and then more or less stabilizes at 7.6% and 6.8% for 5 and 7 L/min, respectively. The simulations can reasonably capture the variation trends of the measured CO mole fraction for these two different flow rates. These results, i.e., the decrease of CO mole fraction in Fig. 4a-e, clearly prove that the formed CO in the plasma

region is largely converted back to CO_2 again in the afterglow area, which is undesirable. Similar results were reported in MW plasma [40]. In the following section, this phenomenon will be explained kinetically based on our model.

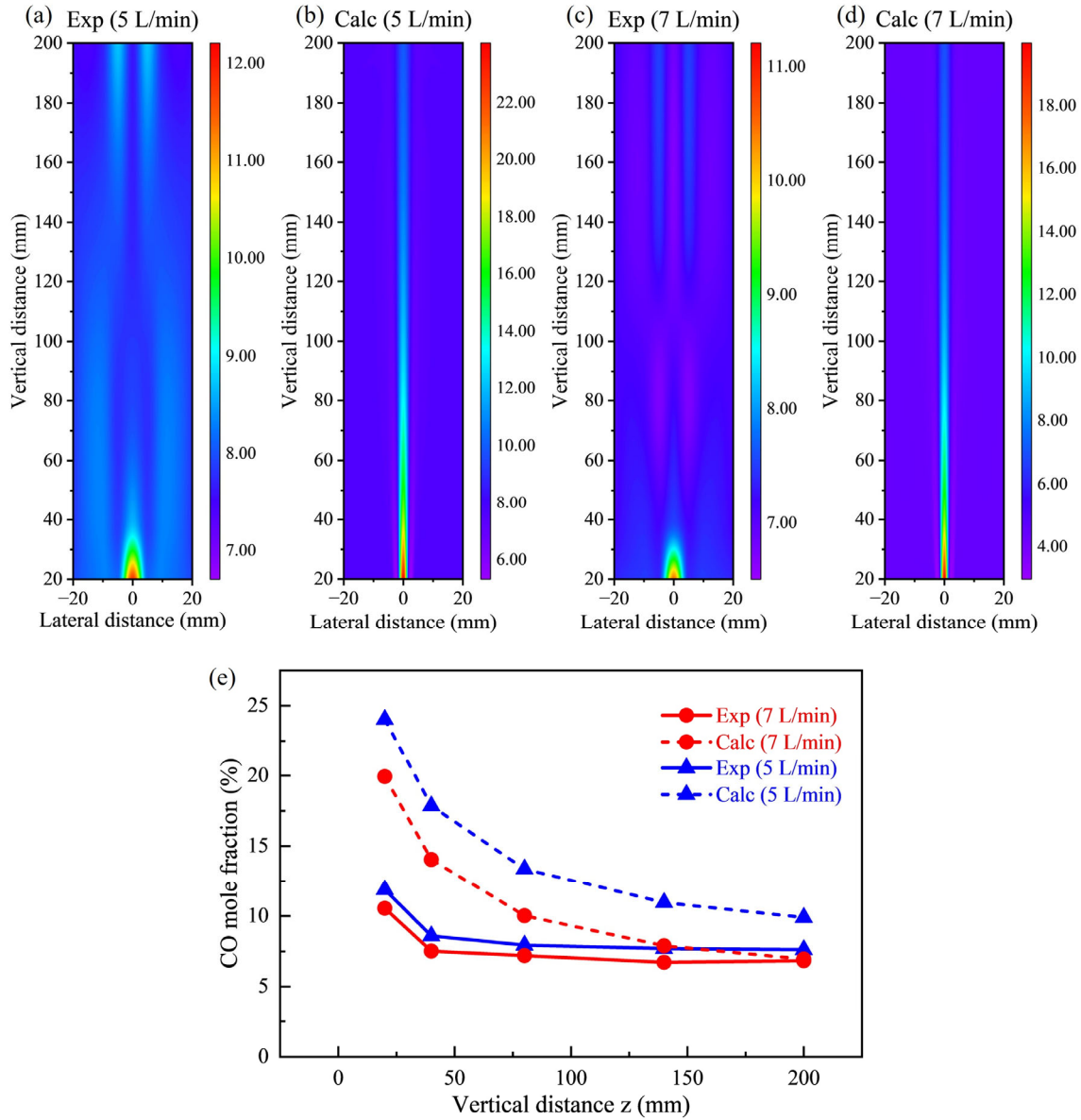


Fig. 4. Comparison of the experimental and calculated CO mole fraction profiles (in %) for 5 L/min and 7 L/min. (a-d): 2D distribution maps; (e): 1D plots at the central axis. (Discharge power: 303 W at 5 L/min and 320 W at 7 L/min)

3.3 Reaction analysis

Our model enables us to investigate the reaction rates of the six thermal reactions incorporated in the model. We have identified that only three of these reactions have significant effect, namely the two CO_2 splitting reactions (reactions 1 and 2 in Table 1), and the O_2 splitting reaction (reaction 4 in Table 1). Indeed, their rates are at least three (and mostly six) orders of magnitude higher than the rates of the other reactions. Our primary focus is on understanding the underlying kinetics of recombination and loss of CO, and therefore we will concentrate in particular on the two CO_2 splitting reactions. The net rates of these two splitting reactions, together with their forward (splitting) and backward (recombination) reaction rates, are given in Figs. 5 and 6, for reaction 1 and 2, respectively, at 5 L/min. In the left plots, the net splitting rates were calculated as the CO_2 dissociation rate minus the recombination rate. For clarity, we focus on the reactor and the start of the exhaust, because most of the conversion and recombination takes place there, due to the higher temperature. Indeed, as mentioned in Section 3.1 above, once the temperature drops below 2000 K, the chemistry becomes more or less “frozen” (i.e., the rates of both splitting and recombination become negligible, as observed indeed in Figs. 5 and 6). Note that the rates for these two reactions at 7 L/min, as well as the spatial distribution of O atom concentrations for both 5 and 7 L/min, which will be used later in our explanation, can be found in Section S3.2 and Figs. S4-S6 in SI.

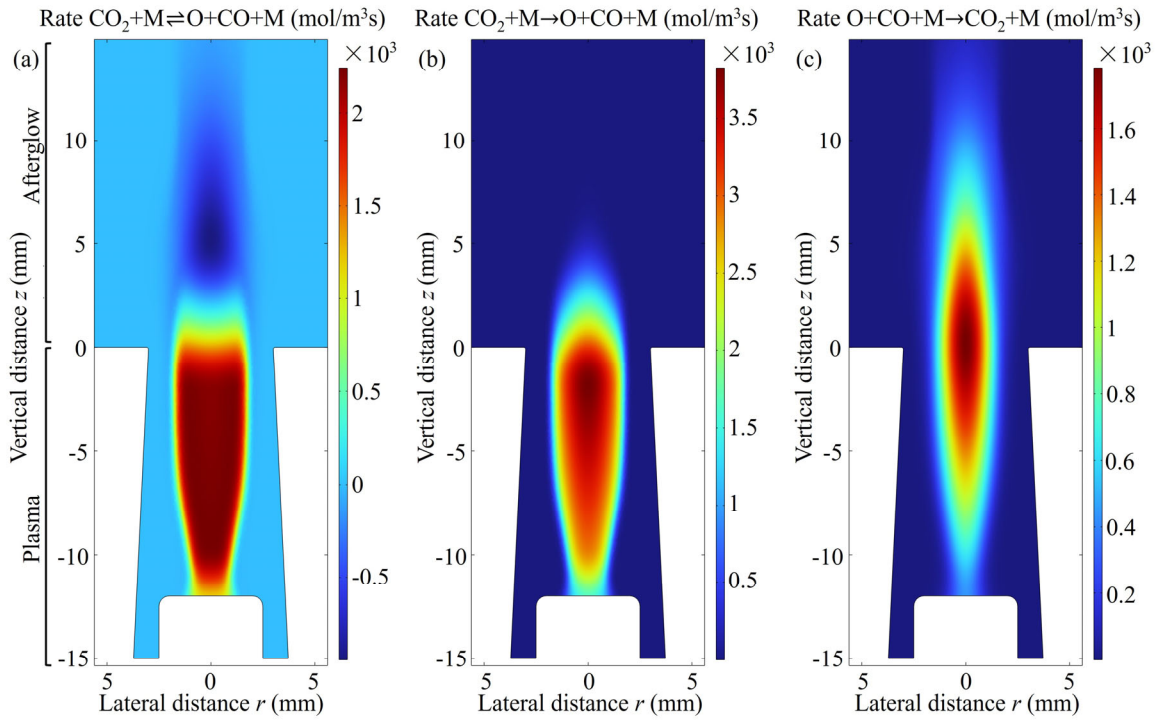


Fig. 5. Net rate of CO_2 conversion by the reaction $\text{CO}_2 + \text{M} \rightleftharpoons \text{O} + \text{CO} + \text{M}$ (a), and its breakdown into the splitting rate (forward reaction) (b) and the recombination rate (backward reaction) (c), at 5 L/min. The plasma is located at $z < 0$ mm, and the afterglow starts when the gas leaves the reactor and enters the exhaust at $z > 0$ mm.

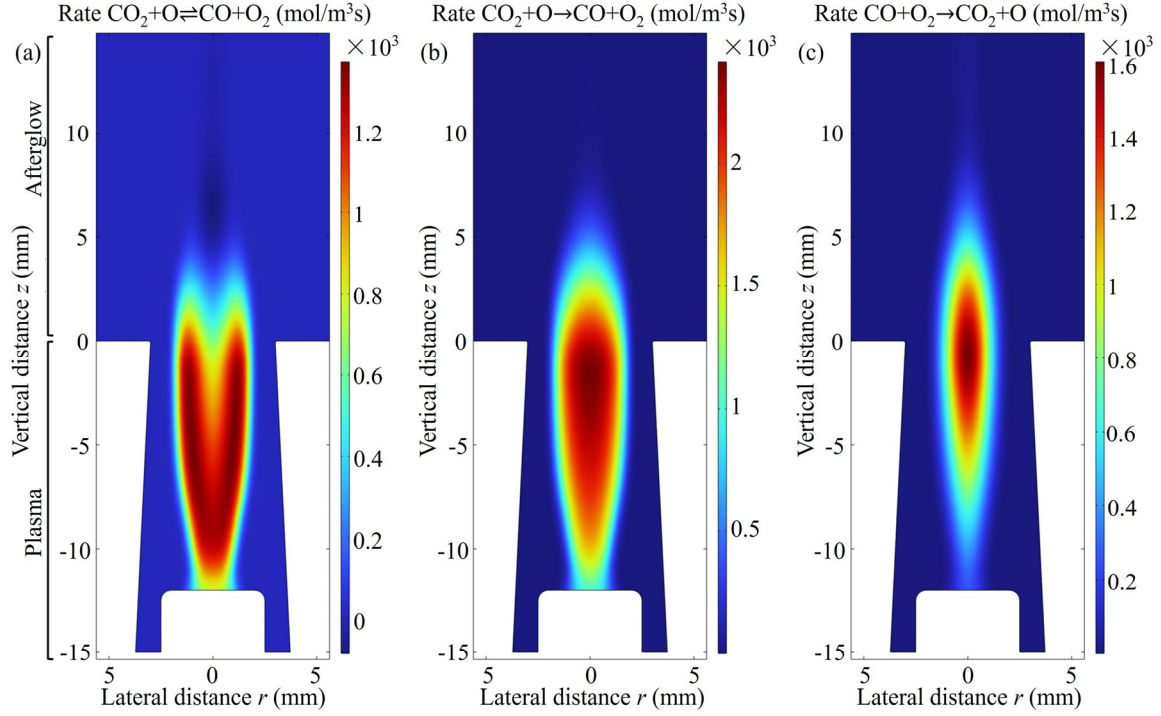


Fig. 6. Net rate of CO_2 conversion by the reaction $\text{CO}_2 + \text{O} \rightleftharpoons \text{CO} + \text{O}_2$ (a), and its breakdown into the splitting rate (forward reaction) (b) and the recombination rate (backward reaction) (c), at 5 L/min. The plasma is located at $z < 0$ mm, and the afterglow starts when the gas leaves the reactor and enters the exhaust at $z > 0$ mm.

By comparing Figs. 5 and 6 (for 5 L/min), we can see that the net reaction rate of CO_2 splitting into CO and O, upon collision with any molecule M, is almost twice as high as the reaction rate of CO_2 splitting into CO and O_2 , upon collision with an O atom. In Ref. [28], a 0D model showed the same relative contribution of both reactions for CO_2 conversion, although not with the same ratio between both rates, at similar (low) specific energy inputs (SEIs) (i.e., 0.5 eV/molecule in [28] and 0.6-0.8 eV/molecule in our case, calculated at 273 K and atmospheric pressure), while reaction 2 became more important at a higher SEI of 4 eV/molecule. The difference in ratio of reaction rates can be explained by the differences between the model used in [28] and our model. These differences include among others: (i) the use of a 0D model (Ref. [28]) vs. a 2D axisymmetric model (this work), (ii) the use of a different chemistry set, i.e., including electron impact reactions (Ref. [28]) vs. assuming thermal chemistry (this work), and (iii) working at different pressures, i.e., 100 mbar (Ref. [28]) vs. atmospheric pressure (this work).

We can also see in Figs. 5 and 6 that both reactions predominantly split CO_2 within the plasma region, whereas the back-reactions forming CO_2 occur in both the plasma and the afterglow region. The

recombination following reaction 2 happens mostly at lower z -values, i.e., inside the plasma and early afterglow (Fig. 6), while the recombination of CO and O through reaction 1 remains more important for a longer distance in the afterglow (Fig. 5), and it is the most important reaction in the exhaust, especially at higher flow rates. This difference in contribution throughout the exhaust can be explained by a difference in recombination rate coefficients between both reactions. In the temperature range between 700 K and 3350 K, the rate coefficient of reaction 1 is always higher than that of reaction 2, but the ratio between both decreases with increasing temperature. Therefore, at higher temperatures, i.e., close to the start of the afterglow and at lower axial distances, the smaller difference between both rate coefficients, in combination with the higher concentration of O₂ compared to O, results in a relatively higher contribution of recombination reaction 2, even though the rate remains smaller than for reaction 1, as can be seen in Fig. 5c and Fig. 6c for 5 L/min, and in Fig. S4c and Fig. S5c for 7 L/min. Further down the afterglow, at higher axial distances, the gas temperature decreases and therefore the ratio of the recombination rate coefficients increases, and the rate coefficient of reaction 2 drops to almost 0 m³/(mol s) below 2000 K. As a result, recombination through reaction 1 becomes much more important, despite the higher concentration of O₂ compared to O. Notably, for reaction 2, the profile of the net recombination rate displays a distinctive shape, with the peak positioned off-axis at higher z -values. This is because the individual dissociation and recombination rates overlap more in comparison to reaction 1. This overlap tends to counterbalance each other along the central axis. This observation demonstrates that both splitting and recombination can occur simultaneously at the same location in the reactor or exhaust at high temperatures. Hence, it is imperative not only to identify where recombination occurs, as presented in Fig. 5c and 6c, but also to pinpoint the regions where recombination surpasses splitting in significance. In these regions, the loss of CO and O₂ becomes prominent, subsequently leading to a reduction in CO₂ conversion.

To delve into a more intricate analysis of the positions where recombination surpasses CO₂ splitting, we present the forward and backward rates of the two CO₂ splitting reactions in Fig. 7, as well as the temperature profile along the symmetry axis, for gas flow rates of 5 and 7 L/min. The intersection points between the dissociation and recombination reactions, and the corresponding temperatures, are indicated for both conditions and each reaction. These transition points signify the juncture where recombination takes precedence over dissociation, and their values are listed in Table 2. One noteworthy observation is that the transition points are always located at a z -value larger than 0 mm, i.e., in the afterglow. So, we can conclude that a net dissociation of CO₂ is predominant within the plasma and recombination prevails in the afterglow, limiting the overall CO₂ conversion. A second conclusion we can draw from Table 2 is that the transition point for reaction 2 consistently has a higher z -value, indicating that reaction 2 gives rise to CO₂ dissociation over a longer spatial distance, albeit not necessarily in greater quantities. This phenomenon stems from the relatively high concentration of O atoms that persists at the inception of the afterglow, as can be seen in the

O concentration map in Section S3.2 of SI (Fig. S6). For example, at 5 L/min, the O atom concentration only drops below 1% of its maximum value at $z = 22.2$ mm on the central axis. The presence of these O atoms at the start of the afterglow contributes to the recombination rate for reaction 1 and the dissociation rate for reaction 2. This elucidates why recombination takes precedence further into the exhaust for reaction 2 compared to reaction 1. The overestimation of the temperature and CO mole fraction in our model compared to the experiments will probably not influence our conclusion. At every temperature along the symmetry axis, for both flow rates, the equilibrium constant, calculated as the splitting rate coefficient over the recombination rate coefficient, is larger for reaction 2 than for reaction 1, indicating the preference for CO₂ splitting in reaction 2 and for recombination in reaction 1, and this difference becomes even larger at lower temperatures (as found in our experiments). In addition, the lower CO mole fraction in our experiments, i.e., the lower conversion, might lead to a lower concentration of O atoms, which determines the recombination rate of reaction 1 and the splitting rate of reaction 2, but it might also lead to a lower concentration of O₂, which determines the recombination rate of reaction 2.

The corresponding temperatures for these transition points are close to 3000 K, as listed in Table 2, except for reaction 2 at 7 L/min. Consistently, a temperature of 3000 K for recombination to take over from CO₂ splitting and thus the conversion decreases, was also reported in a modelling study for a MW reactor [30]. Only at 7 L/min for reaction 2, the temperature of this transition point deviates more from 3000 K. The position of this transition depends not only on the concentrations of the different species, which inherently influence the reaction rates, but also on the flow rate that transports these species and heat through the reactor and exhaust. This trend is evident in Table 2: the z -value of the transition points increases for both reactions with increasing flow rate. However, because the recombination of reaction 2 takes precedence over splitting quite distantly into the exhaust at 7 L/min, the gas at this transition point undergoes more substantial cooling due to heat dissipation by the heat sink, thus leading to a lower temperature. This phenomenon highlights the complex interplay between flow rates, reaction kinetics, and temperature profiles in this system. Note that due to an overestimate of the simulated temperature, as presented in Section 3.1 above, the real transition points might be closer to the plasma area (a lower z -value) in comparison to the model predictions. In addition, it might be argued that the differences in vertical position and temperature of the transition points relative to each other as a function of the flow rate are not statistically significant, considering the overestimation of the temperature and CO mole fraction in the model compared to the experiments. However, the decreasing trends along the symmetry axis for both the temperature and the CO mole fraction are similar in the model and the experiments. The rather similar temperature for 5 L/min and 7 L/min and the lower CO mole fraction for 7 L/min compared to 5 L/min can be observed for both the model and the experiments. These similar trends will then result in similar trends in the transition points. Still, this paragraph aims to indicate the very close temperature values of the transition points around 3000 K

and explain the deviation of one of these points using its vertical distance, and not to prove the trends as function of the flow rate.

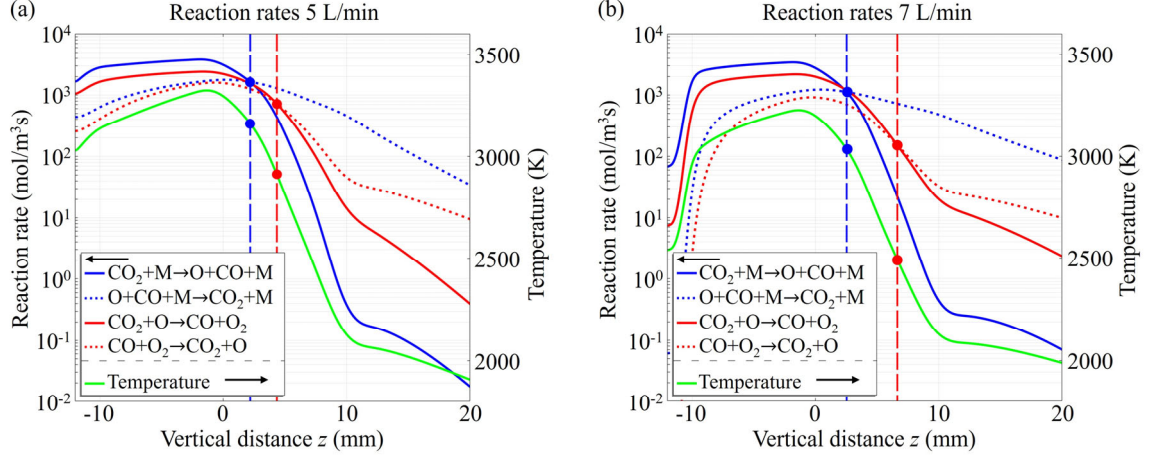


Fig. 7. Splitting rates (solid lines) and recombination rates (dotted lines) of the two main CO_2 dissociation reactions, as well as the temperature (green, right y-axis) along the symmetry axis, for 5 L/min (a) and 7 L/min (b). The transition points at which recombination becomes more important than CO_2 splitting (higher rate) and their corresponding gas temperature are indicated (see also Table 2).

Table 2. Overview of the transition points where recombination takes precedence over dissociation on the symmetry axis for the two CO_2 conversion reactions, at the two different flow rates, together with the corresponding temperature (model results).

Flow rate (L/min)	Reaction	Vertical distance of the transition points (z, mm)	Temperature (K)
5	$\text{CO}_2 + \text{M} \rightleftharpoons \text{O} + \text{CO} + \text{M}$	2.19	3159
	$\text{CO}_2 + \text{O} \rightleftharpoons \text{CO} + \text{O}_2$	4.35	2913
7	$\text{CO}_2 + \text{M} \rightleftharpoons \text{O} + \text{CO} + \text{M}$	2.54	3035
	$\text{CO}_2 + \text{O} \rightleftharpoons \text{CO} + \text{O}_2$	6.65	2493

The results presented above offer a compelling insight: by rapidly cooling the gas after it passes the transition points in the afterglow, to temperatures where the reaction rates are negligibly small, we hypothesize it becomes feasible to significantly inhibit the recombination reactions. Consequently, this inhibition of recombination could lead to a substantial enhancement in CO_2 conversion. In previous work on a MW plasma, a limit of 2000 K was reported under which the temperature needs to drop to “stop” the reactions and obtain a final CO_2 conversion that does not change anymore, based on the calculated

equilibrium composition of CO_2 and its dissociation products [9,29,30]. In our work, the experimental results plotted in Figs. 3 and 4 show that the CO_2 conversion stabilizes only after the gas temperature has dropped to approximately 700 K, so to make sure that we retain the highest conversion possible, we should try to quickly decrease the temperature to a value as low as possible, below 2000 K or preferably below 700 K.

3.4 Demonstration of afterglow quenching for enhanced performance

To demonstrate the above proposed strategy of quenching the afterglow region for enhanced performance, we developed a plasmatron reactor with cooling system, as depicted in Fig. 8. Two cooling stages: upstream (closer to plasma) and downstream (see Fig. 8a), were meticulously designed to explore how the position of quenching influences the overall reaction performance. The cooling was implemented by utilizing two separate water jackets, each filled with circulating water, with water ($\sim 298\text{K}$) flowing in from the bottom and exiting from the top. Two thermocouples were positioned at around $z = 20\text{ mm}$ and $z = 100\text{ mm}$ within the afterglow region to measure the gas temperatures at the two cooling stages. Unlike the previous experiments, we only sampled and analysed the exhaust gas in this section. Note that the reactor designed in this section differs from the reactor used in the above sections, as it was specifically designed to showcase and validate the proposed strategy.

In the absence of cooling, the afterglow region exhibits a notable blue flame extending to approximately 120 mm, as depicted in Fig. 8b. This phenomenon is indicative, presumably, of vigorous CO recombination into CO_2 . However, with the introduction of the cooling system, as illustrated in Fig. 8c, the flame almost entirely vanishes. This dramatic change suggests a potent inhibition of the CO recombination reactions due to the cooling mechanism. Experimental results showed that the discharge power remained essentially unchanged before and after cooling for different conditions, indicating that the discharge itself was not notably affected by cooling. It can be therefore inferred that mainly the afterglow region was affected by cooling, leading to the disappearance of the blue flame.

As evident from the time-resolved gas temperature measurements for the two cooling stages illustrated in Fig. 9, quenching exerts a significant influence on the afterglow gas temperatures and the overall stabilization of plasma operation. The stabilized temperatures for both the upstream and downstream stages experience a remarkable drop: from 1500 K to 980 K, and from 1160 K to 650 K, respectively. Also, it is intriguing to observe that the startup time required for temperature stabilization is significantly shorter: from around 150 s without cooling to ca. 25 s with cooling.

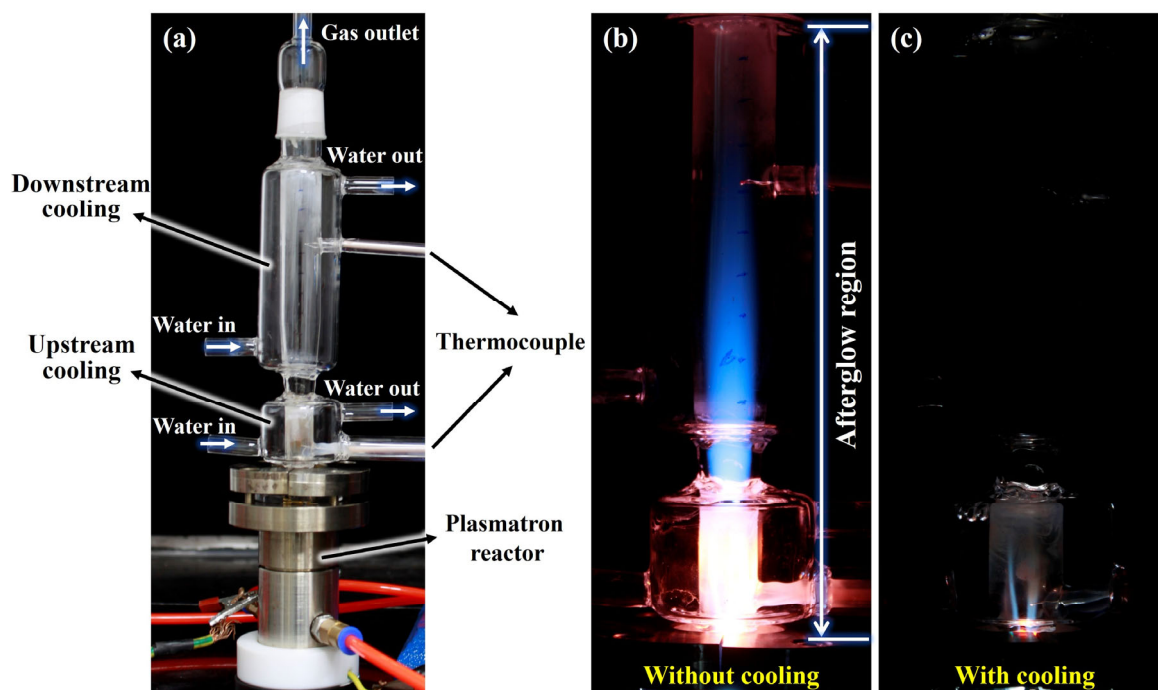


Fig. 8. Picture of the plasmatron reactor with afterglow quenching (a), and photograph of the afterglow region without cooling (b) and with cooling implemented (c). CO₂ flow rate: 5 L/min, discharge power: 445W.

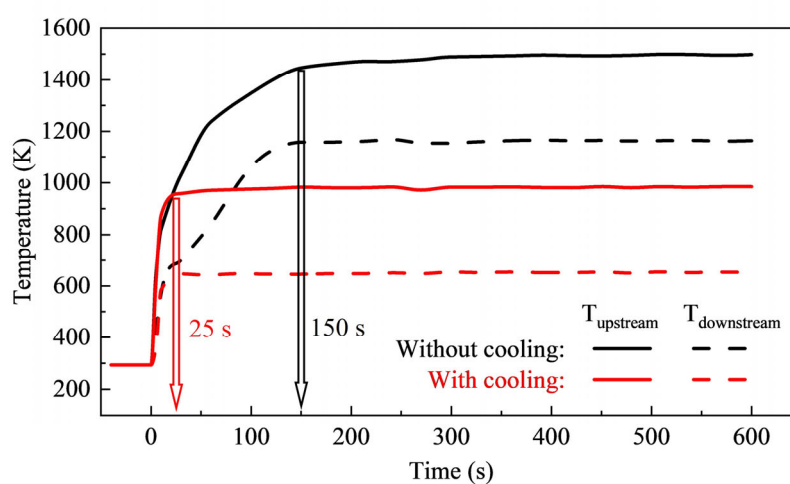


Fig. 9. Time-resolved measurements of gas temperatures for the two cooling stages (T_{upstream} , $T_{\text{downstream}}$), with and without cooling implemented (both stages). The point at which the temperature stabilizes is indicated.

The impact of afterglow quenching, achieved through solely upstream or downstream cooling, and both, on the CO₂ conversion and energy efficiency is illustrated in Fig. 10. Initially, the CO₂ conversion increases

with rising flow rates, followed by a decline, while the energy efficiency exhibits a continuous upward trend. These trends are consistent with prior research and can be attributed to a combination of factors, such as residence time, SEI, and gas temperature [25,27,41]. As evident from Fig. 10, afterglow quenching yields a substantial enhancement in reaction performance, particularly at lower flow rates between 2 to 5 L/min. Cooling the upstream stage, which is in closer proximity to the plasma region and features higher gas temperatures, results in a more significant improvement compared to cooling the downstream stage alone. For instance, at 3 L/min, the CO₂ conversion can be augmented from 6.6% to 13.4% (an enhancement by a factor two) with downstream cooling, and to 17.6% (a factor 2.6 enhancement) with upstream cooling, and further to 19.5% (an enhancement of nearly a factor three) with both upstream and downstream cooling. This observation is logical, as early cooling in the afterglow region can effectively restrict recombination reactions to a greater degree.

The energy efficiency also experiences a remarkable enhancement due to afterglow quenching, albeit to a slightly lesser degree than the CO₂ conversion (see Fig. 10). At a flow rate of 3 L/min, it increases from 13.5% to 20.9% (a factor 1.5 enhancement) with downstream cooling, and to 26.5% (an enhancement of nearly a factor two) with upstream cooling, and further to 28.5% (an enhancement by a factor 2.1) with both upstream and downstream cooling. It is worth noting that the maximum energy efficiency achieved in this study (36.4% at 6 L/min with two-stage cooling) surpasses the majority of atmospheric pressure plasma-assisted CO₂ splitting works [32]. The remaining energy is presumed to be partly utilized for gas heating (estimated to be 56%, see Section S4 in SI), with the remainder dissipating in various forms (not directly heating the feed gas), such as light emission, transfer to the electrodes, and dispersion through the outer surface of the reactor into the surrounding environment.

The efficacy of cooling diminishes considerably as the flow rates increase, as observed in Fig. 10, for both CO₂ conversion and energy efficiency. This reduction can be largely attributed to the higher gas flow rate, diminishing the cooling effectiveness of the water jackets, which operate at a constant circulating water rate.

The results presented in this section unequivocally demonstrate the effectiveness and significance of afterglow quenching in improving the CO₂ splitting performance, even up to a factor three, for warm plasmas.

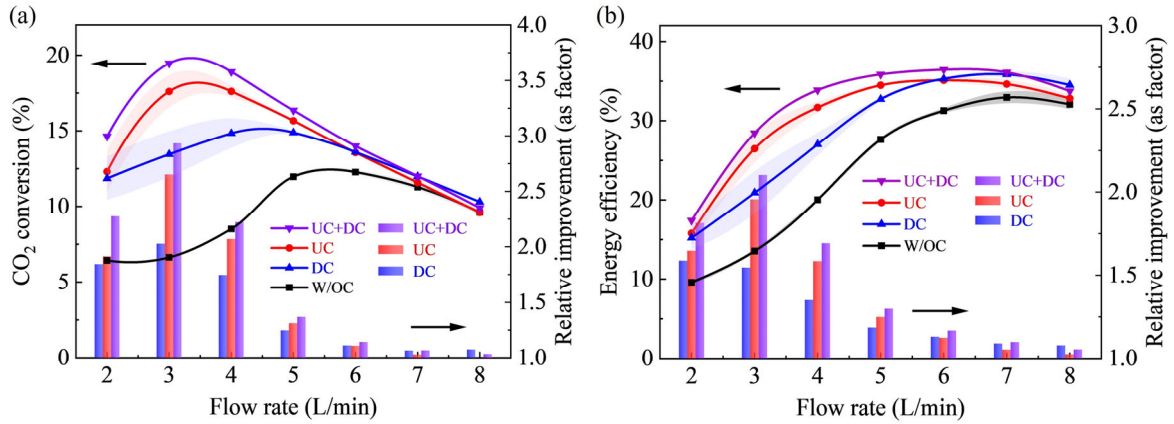


Fig. 10. CO₂ conversion (a) and energy efficiency (b) of the plasmatron reactor under four different cooling conditions: without cooling (W/OC; black), solely upstream cooling (UC; red), solely downstream cooling (DC; blue), and with both upstream and downstream cooling (UC+DC; purple), as a function of flow rate, ranging from 2 to 8 L/min. Each condition was repeated three times and the plotted data represents the mean value with error bands. The bar charts additionally illustrate the relative improvement (see Section S4 for the definition) in CO₂ conversion (a) and energy efficiency (b) achieved using the different cooling conditions, i.e., UC (red), DC (blue), and UC+DC (purple).

4. Conclusions

In this study, we investigated in detail the recombination reactions (of CO + O/O₂) in the CO₂ splitting process in an atmospheric plasmatron reactor. We developed an innovative *in-situ* gas sampling method, which allows us to visualize the 2D spatial distribution of gas product compositions experimentally. In addition, we developed a 2D axisymmetric fluid dynamics + reaction kinetics model that incorporates CO₂ splitting chemistry, and we validated it against our experimental data. Subsequently, we analysed the spatially resolved reaction rates to unveil the competition between CO₂ dissociation and (CO + O/O₂) recombination reactions in both plasma and afterglow region. Finally, to validate the proposed afterglow quenching strategy for performance optimization, we constructed a plasmatron equipped with a two-stage cooling system for the CO₂ splitting reactions.

Our results unequivocally confirm the significant role of recombination reactions in the afterglow, thereby limiting the performance of plasma-based CO₂ splitting. For instance, at a flow rate of 5 L/min, the measured CO mole fraction drops significantly from 11.9% at a vertical distance of $z = 20$ mm in the afterglow region to 8.6% at $z = 40$ mm. Moreover, the CO₂ conversion stabilizes along the flow rate direction only when the gas temperature drops to approximately 700 K. Our 2D axisymmetric model qualitatively reproduces the drop in temperature and CO mole fraction along the flow direction. Reaction rate analysis reveals the

importance of two reactions, i.e., $CO_2 + M \rightleftharpoons O + CO + M$ and $CO_2 + O \rightleftharpoons CO + O_2$ in plasma-based CO_2 splitting, with their significance varying along the flow rate direction. The forward reactions dominate within the plasma region, contributing to CO_2 conversion, while the recombination reactions take precedence in the afterglow region, limiting the overall CO_2 conversion.

We validate the proposed afterglow quenching strategy for performance optimization using a specially designed plasmatron reactor with a two-stage cooling system. This approach leads to a dramatic increase in both CO_2 conversion and energy efficiency, particularly at low flow rates. For instance, at 3 L/min, the CO_2 conversion increases from 6.6% to 19.5% (i.e., an enhancement by nearly a factor three), while the energy efficiency rises from 13.5% to 28.5% (a factor 2.1 enhancement) with afterglow cooling, accompanied by a substantial reduction in startup time, from approximately 150 s (without cooling) to only 25 s (with cooling). Furthermore, the segmented cooling system underscores the significance of early quenching in inhibiting recombination reactions within the afterglow region.

In summary, our work emphasizes and demonstrates the importance of inhibiting recombination reactions in plasma-based CO_2 conversion through a combination of experiments and modelling. This provides critical insights into practical strategies for enhancing the performance in plasma-based CO_2 conversion, not only for the plasma reactor under study here, but also for other types of warm plasmas.

Acknowledgement

This work was supported by the National Natural Science Foundation of China [No. 52276214 and No. 51976191]; the "Pioneer" and "Leading Goose" R&D Program of Zhejiang Province [No. 2023C03129]; the Fund for Scientific Research (FWO) [Grant No. 1101522N]; and the European Research Council (ERC) under the European Union's Horizon 2020 research and innovation programme [Grant Agreement No. 810182 – SCOPE ERC Synergy project, and grant agreement No. 101081162 – PREPARE ERC Proof of Concept project]. The computational resources and services used in this work were provided by the HPC core facility CalcUA of the Universiteit Antwerpen, and VSC (Flemish Supercomputer Center), funded by the Research Foundation - Flanders (FWO) and the Flemish Government.

References

- [1] IPCC, 2023: Climate Change 2023: Synthesis Report, Contribution of Working Groups I, II and III to the Sixth Assessment Report of the Intergovernmental Panel on Climate Change [Core Writing Team, H. Lee and J. Romero (eds.)], IPCC, Geneva, Switzerland. <https://doi.org/10.59327/IPCC/AR6-9789291691647>.
- [2] S. Dang, B. Qin, Y. Yang, H. Wang, J. Cai, Y. Han, S. Li, P. Gao, Y. Sun, Rationally designed indium oxide catalysts for CO_2 hydrogenation to methanol with high activity and selectivity, *Sci. Adv.* 6 (2020). <http://doi.org/10.1126/sciadv.aaz2060>.
- [3] M. Liu, Y. Pang, B. Zhang, P. De Luna, O. Voznyy, J. Xu, X. Zheng, C.T. Dinh, F. Fan, C. Cao, F.P.G. de Arquer, T.S. Safaei, A. Mepham, A. Klinkova, E. Kumacheva, T. Filleter, D. Sinton, S.O. Kelley, E.H. Sargent,

- Enhanced electrocatalytic CO₂ reduction via field-induced reagent concentration, *Nature* 537 (2016) 382-386. <http://doi.org/10.1038/nature19060>.
- [4] J. Artz, T.E. Mueller, K. Thenert, J. Kleinekorte, R. Meys, A. Sternberg, A. Bardow, W. Leitner, Sustainable conversion of carbon dioxide: an integrated review of catalysis and life cycle assessment, *Chem. Rev.* 118 (2018) 434-504. <http://doi.org/10.1021/acs.chemrev.7b00435>.
- [5] H. Xu, J. Ma, P. Tan, Z. Wu, Y. Zhang, M. Ni, J. Xuan, Enabling thermal-neutral electrolysis for CO₂-to-fuel conversions with a hybrid deep learning strategy, *Energy Conv. Manag.* 230 (2021). <http://doi.org/10.1016/j.enconman.2021.113827>.
- [6] J. Gu, C. Hsu, L. Bai, H.M. Chen, X. Hu, Atomically dispersed Fe³⁺ sites catalyze efficient CO₂ electroreduction to CO, *Science* 364 (2019) 1091-1094. <http://doi.org/10.1126/science.aaw7515>.
- [7] K. Niu, Y. Xu, H. Wang, R. Ye, H.L. Xin, F. Lin, C. Tian, Y. Lum, K.C. Bustillo, M.M. Doeff, M.T.M. Koper, J. Ager, R. Xu, H. Zheng, A spongy nickel-organic CO₂ reduction photocatalyst for nearly 100% selective CO production, *Sci. Adv.* 3 (2017). <http://doi.org/10.1126/sciadv.1700921>.
- [8] M. Schreier, F. Heroguel, L. Steier, S. Ahmad, J.S. Luterbacher, M.T. Mayer, J. Luo, M. Gratzel, Solar conversion of CO₂ to CO using Earth-abundant electrocatalysts prepared by atomic layer modification of CuO, *Nat. Energy* 2 (2017). <http://doi.org/10.1038/nenergy.2017.87>.
- [9] R. Snoeckx, A. Bogaerts, Plasma technology - a novel solution for CO₂ conversion? *Chem. Soc. Rev.* 46 (2017) 5805-5863. <http://doi.org/10.1039/c6cs00066e>.
- [10] O.S. Bushuyev, P. De Luna, T.D. Cao, L. Tao, G. Saur, J. van de Lagemaat, S.O. Kelley, E.H. Sargent, What should we make with CO₂ and how can we make it? *Joule* 2 (2018) 825-832. <http://doi.org/10.1016/j.joule.2017.09.003>.
- [11] B. Zhao, Y. Su, Process effect of microalgal-carbon dioxide fixation and biomass production: A review, *Renew. Sust. Energ. Rev.* 31 (2014) 121-132. <http://doi.org/10.1016/j.rser.2013.11.054>.
- [12] Y. Qiu, L. Ma, M. Li, D. Cui, S. Zhang, D. Zeng, R. Xiao, Copper and cobalt co-doped ferrites as effective agents for chemical looping CO₂ splitting, *Chem. Eng. J.* 387 (2020). <http://doi.org/10.1016/j.cej.2020.124150>.
- [13] E. Koepf, I. Alxneit, C. Wieckert, A. Meier, A review of high temperature solar driven reactor technology: 25 years of experience in research and development at the Paul Scherrer Institute, *Appl. Energy* 188 (2017) 620-651. <http://doi.org/10.1016/j.apenergy.2016.11.088>.
- [14] L. Zhu, Microalgal culture strategies for biofuel production: a review, *Biofuels Bioprod. Biorefining* 9 (2015) 801-814. <http://doi.org/10.1002/bbb.1576>.
- [15] L. Han, S. Dong, E. Wang, Transition-metal (Co, Ni, and Fe)-based electrocatalysts for the water oxidation reaction, *Adv. Mater.* 28 (2016) 9266-9291. <http://doi.org/10.1002/adma.201602270>.
- [16] J. Fukushima, M. Tanaka, S. Takayama, H. Takizawa, Kinetics of CO₂ splitting by microwave irradiation using honeycomb-like pellets of Fe₃O₄/FeO, *Chem. Eng. J.* 428 (2022). <http://doi.org/10.1016/j.cej.2021.131087>.
- [17] A. George, B. Shen, M. Craven, Y. Wang, D. Kang, C. Wu, X. Tu, A review of non-thermal plasma technology: a novel solution for CO₂ conversion and utilization, *Renew. Sust. Energ. Rev.* 135 (2021) 109702. <http://doi.org/10.1016/j.rser.2020.109702>.
- [18] G. Chen, X. Tu, G. Himm, A. Weidenkaff, Plasma pyrolysis for a sustainable hydrogen economy, *Nat. Rev. Mater.* 7 (2022) 333-334. <http://doi.org/10.1038/s41578-022-00439-8>.
- [19] L. Hollevoet, F. Jardali, Y. Gorbaney, J. Creel, A. Bogaerts, J.A. Martens, Towards green ammonia synthesis through plasma-driven nitrogen oxidation and catalytic reduction, *Angew. Chem.-Int. Edit.* 132 (2020) 24033-24037. <http://doi.org/10.1002/anie.202011676>.
- [20] S. Kelly, A. Bogaerts, Nitrogen fixation in an electrode-free microwave plasma, *Joule* 5 (2021) 3006-3030. <http://doi.org/10.1016/j.joule.2021.09.009>.
- [21] Y. Wang, W. Yang, S. Xu, S. Zhao, G. Chen, A. Weidenkaff, C. Hardacre, X. Fan, J. Huang, X. Tu, Shielding protection by mesoporous catalysts for improving plasma-catalytic ambient ammonia synthesis, *J. Am. Chem. Soc.* 144 (2022) 12020-12031. <http://doi.org/10.1021/jacs.2c01950>.
- [22] A. Salden, M. Budde, C.A. Garcia-Soto, O. Biondo, J. Barauna, M. Faedda, B. Musig, C. Fromentin, M. Nguyen-Quang, H. Philpott, G. Hasrack, D. Aceto, Y. Cai, F.A. Jury, A. Bogaerts, P. Da Costa, R. Engeln, M.E. Gálvez, T. Gans, T. Garcia, V. Guerra, C. Henriques, M. Motak, M.V. Navarro, V.I. Parvulescu, G. Van Rooij, B. Samojeden, A. Sobota, P. Tosi, X. Tu, O. Guaitella, Meta-analysis of CO₂ conversion, energy efficiency, and other performance data of plasma-catalysis reactors with the open access PIONEER database, *J. Energy Chem.* 86 (2023) 318-342. <http://doi.org/10.1016/j.jechem.2023.07.022>.
- [23] B. Wanten, R. Vertongen, R. De Meyer, A. Bogaerts, Plasma-based CO₂ conversion: How to correctly analyze the performance? *J. Energy Chem.* 86 (2023) 180-196. <http://doi.org/10.1016/j.jechem.2023.07.005>.
- [24] A. Bogaerts, G. Centi, Plasma technology for CO₂ conversion: A personal perspective on prospects and gaps,

- Front. Energy Res. 8 (2020). <http://doi.org/10.3389/fenrg.2020.00111>.
- [25] H. Zhang, Q. Tan, Q. Huang, K. Wang, X. Tu, X. Zhao, C. Wu, J. Yan, X. Li, Boosting the conversion of CO₂ with biochar to clean CO in an atmospheric plasmatron: a synergy of plasma chemistry and thermochemistry, *ACS Sustain. Chem. Eng.* 10 (2022) 7712-7725. <http://doi.org/10.1021/acssuschemeng.2c01778>.
- [26] H. Zhang, L. Li, R. Xu, J. Huang, N. Wang, X. Li, X. Tu, Plasma-enhanced catalytic activation of CO₂ in a modified gliding arc reactor, *Waste Disposal & Sustainable Energy* 2 (2020) 139-150. <http://doi.org/10.1007/s42768-020-00034-z>.
- [27] L. Li, H. Zhang, X. Li, J. Huang, X. Kong, R. Xu, X. Tu, Magnetically enhanced gliding arc discharge for CO₂ activation, *J. CO₂ Util.* 35 (2020) 28-37. <http://doi.org/10.1016/j.jcou.2019.08.021>.
- [28] V. Vermeiren, A. Bogaerts, Plasma-based CO₂ conversion: to quench or not to quench? *J. Phys. Chem. C* 124 (2020) 18401-18415. <http://doi.org/10.1021/acs.jpcc.0c04257>.
- [29] E.R. Mercer, S. Van Alphen, C.F.A.M. van Deursen, T.W.H. Righart, W.A. Bongers, R. Snyders, A. Bogaerts, M.C.M. van de Sanden, F.J.J. Peeters, Post-plasma quenching to improve conversion and energy efficiency in a CO₂ microwave plasma, *Fuel* 334 (2023). <http://doi.org/10.1016/j.fuel.2022.126734>.
- [30] S. Van Alphen, A. Hecimovic, C.K. Kiefer, U. Fantz, R. Snyders, A. Bogaerts, Modelling post-plasma quenching nozzles for improving the performance of CO₂ microwave plasmas, *Chem. Eng. J.* 462 (2023). <http://doi.org/10.1016/j.cej.2023.142217>.
- [31] J. Li, X. Zhang, J. Shen, T. Ran, P. Chen, Y. Yin, Dissociation of CO₂ by thermal plasma with contracting nozzle quenching, *J. CO₂ Util.* 21 (2017) 72-76. <http://doi.org/10.1016/j.jcou.2017.04.003>.
- [32] R. Vertongen, A. Bogaerts, How important is reactor design for CO₂ conversion in warm plasmas? *J. CO₂ Util.* 72 (2023) 102510. <http://doi.org/10.1016/j.jcou.2023.102510>.
- [33] A. van de Steeg, P. Viegas, A. Silva, T. Butterworth, A. van Bavel, J. Smits, P. Diomedea, M. van de Sanden, G. van Rooij, Redefining the microwave plasma-mediated CO₂ reduction efficiency limit: the role of O-CO₂ association, *ACS Energy Lett.* 6 (2021) 2876-2881. <http://doi.org/10.1021/acsenenergylett.1c01206>.
- [34] A. Hecimovic, F.A. D Isa, E. Carbone, U. Fantz, Enhancement of CO₂ conversion in microwave plasmas using a nozzle in the effluent, *J. CO₂ Util.* 57 (2022) 101870. <http://doi.org/https://doi.org/10.1016/j.jcou.2021.101870>.
- [35] W. Bongers, H. Bouwmeester, B. Wolf, F. Peeters, S. Welzel, D. van den Bekerom, N. den Harder, A. Goede, M. Graswinckel, P.W. Groen, J. Kopecki, M. Leins, G. van Rooij, A. Schulz, M. Walker, R. van de Sanden, Plasma-driven dissociation of CO₂ for fuel synthesis, *Plasma Process. Polym.* 14 (2017) 1600126. <http://doi.org/https://doi.org/10.1002/ppap.201600126>.
- [36] H. Kim, S. Song, C.P. Tom, F. Xie, Carbon dioxide conversion in an atmospheric pressure microwave plasma reactor: Improving efficiencies by enhancing afterglow quenching, *J. CO₂ Util.* 37 (2020) 240-247. <http://doi.org/https://doi.org/10.1016/j.jcou.2019.12.011>.
- [37] A. Hecimovic, C.K. Kiefer, A. Meindl, R. Antunes, U. Fantz, Fast gas quenching of microwave plasma effluent for enhanced CO₂ conversion, *J. CO₂ Util.* 71 (2023) 102473. <http://doi.org/https://doi.org/10.1016/j.jcou.2023.102473>.
- [38] G. Chen, F. Buck, I. Kistner, M. Widenmeyer, T. Schiestel, A. Schulz, M. Walker, A. Weidenkaff, A novel plasma-assisted hollow fiber membrane concept for efficiently separating oxygen from CO in a CO₂ plasma, *Chem. Eng. J.* 392 (2020) 123699. <http://doi.org/https://doi.org/10.1016/j.cej.2019.123699>.
- [39] G. Chen, M. Widenmeyer, X. Yu, N. Han, X. Tan, G. Homm, S. Liu, A. Weidenkaff, Perspectives on achievements and challenges of oxygen transport dual-functional membrane reactors, *J. Am. Ceram. Soc.* (2023). <http://doi.org/https://doi.org/10.1111/jace.19411>.
- [40] K. Wiegers, A. Schulz, M. Walker, G.E.M. Tovar, Determination of the Conversion and Efficiency for CO₂ in an Atmospheric Pressure Microwave Plasma Torch, *Chem. Ing. Tech.* 94 (2022) 299-308. <http://doi.org/https://doi.org/10.1002/cite.202100149>.
- [41] J. Huang, H. Zhang, Q. Tan, L. Li, R. Xu, Z. Xu, X. Li, Enhanced conversion of CO₂ into O₂-free fuel gas via the Boudouard reaction with biochar in an atmospheric plasmatron, *J. CO₂ Util.* 45 (2021). <http://doi.org/10.1016/j.jcou.2020.101429>.
- [42] F. Seibold, P. Ligrani, B. Weigand, Flow and heat transfer in swirl tubes-A review, *Int. J. Heat Mass Transf.* 187 (2022). <http://doi.org/10.1016/j.ijheatmasstransfer.2021.122455>.
- [43] D.J. Jin, H.S. Uhm, G. Cho, Influence of the gas-flow Reynolds number on a plasma column in a glass tube, *Phys. Plasmas* 20 (2013). <http://doi.org/10.1063/1.4819246>.
- [44] S. Van Alphen, H.A. Eshtehardi, C. O'Modhrain, J. Bogaerts, H. Van Poyer, J. Creel, M. Delplancke, R. Snyders, A. Bogaerts, Effusion nozzle for energy-efficient NO_x production in a rotating gliding arc plasma reactor, *Chem. Eng. J.* 443 (2022). <http://doi.org/10.1016/j.cej.2022.136529>.
- [45] G. Trenchev, S. Kolev, W. Wang, M. Ramakers, A. Bogaerts, CO₂ conversion in a gliding arc plasmatron:

- multidimensional modeling for improved efficiency, *J. Phys. Chem. C*. 121 (2017) 24470-24479. <http://doi.org/10.1021/acs.jpcc.7b08511>.
- [46] T.P. Nunnally, Application of Low Current Gliding Arc Plasma Discharges for Hydrogen Sulfide Decomposition and Carbon Dioxide Emission Reduction, Drexel University, 2011.
- [47] A. Fridman, Plasma Chemistry, Cambridge University Press, Cambridge, 2008.
- [48] J. Liu, X. Wang, X. Li, B. Likozar, A. Zhu, CO₂ conversion, utilisation and valorisation in gliding arc plasma reactors, *J. Phys. D-Appl. Phys.* 53 (2020). <http://doi.org/10.1088/1361-6463/ab7c04>.
- [49] J. Liu, X. Li, J. Liu, A. Zhu, Insight into gliding arc (GA) plasma reduction of CO₂ with H₂: GA characteristics and reaction mechanism, *J. Phys. D-Appl. Phys.* 52 (2019). <http://doi.org/10.1088/1361-6463/ab1bb1>.
- [50] V. Aubrecht, M. Bartlova, Radiation transfer in thermal plasmas of air, N₂ and CO₂, 2008 17th International Conference on Gas Discharges and Their Applications, 2008, pp. 393-396.
- [51] G.P. Smith, D.M. Golden, M. Fenklach, N.W. Moriarty, B. Eiteneer, M. Goldenberg, C.T. Bowman, R.K. Hanson, S. Song, W.C. Gardiner Jr., V.V. Lissianski, Z. Qin, GRI-Mech 3.0, <http://combustion.berkeley.edu/gri-mech/version30/text30.html>.
- [52] A. Berthelot, A. Bogaerts, Modeling of plasma-based CO₂ conversion: lumping of the vibrational levels, *Plasma Sources Science and Technology* 25 (2016) 45022. <http://doi.org/10.1088/0963-0252/25/4/045022>.
- [53] N. Hansen, T.A. Cool, P.R. Westmoreland, K. Kohse-Hoeinghaus, Recent contributions of flame-sampling molecular-beam mass spectrometry to a fundamental understanding of combustion chemistry, *Prog. Energy Combust. Sci.* 35 (2009) 168-191. <http://doi.org/10.1016/j.pecs.2008.10.001>.

Supplementary Information

Inhibiting recombination to improve the performance of plasma-based CO₂ conversion

Kaiyi Wang^{a,1}, Sara Ceulemans^{b,1}, Hao Zhang^{a,c,*}, Ivan Tsonev^b, Yilin Zhang^a, Yanhui Long^a, Mengxiang Fang^c, Xiaodong Li^a, Jianhua Yan^a, Annemie Bogaerts^{b,*}

a. State Key Laboratory of Clean Energy Utilization, Zhejiang University, Hangzhou 310027, China

b. Research group PLASMANT, Department of Chemistry, University of Antwerp, Wilrijk-Antwerp BE-2610, Belgium

c. Zhejiang University Qingshanhu Energy Research Center, 311305 Hangzhou, P. R. China

¹. These authors contributed equally to this work.

* Corresponding authors:

zhang_hao@zju.edu.cn (H. Zhang);

annemie.bogaerts@uantwerpen.be (A. Bogaerts)

Table of contents

S1 Experimental setup	2
S2 Model description	3
S2.1 Gas flow	3
S2.2 Heat transfer	5
S2.3 Chemistry and transport of chemical species	7
S3 Detailed calculation results	12
S3.1 Gas flow pattern in the reactor and exhaust	12
S3.2 Reaction analysis	13
S4 Afterglow quenching	16
References	17

S1 Experimental setup

A schematic of the experimental setup is presented in Fig. S1, consisting of gas feeding system, power supply, plasmatron reactor with gas sampling set, oscilloscope with high-voltage probe and current probe for electrical parameter measurement, and gas analyser for gas composition analysis.

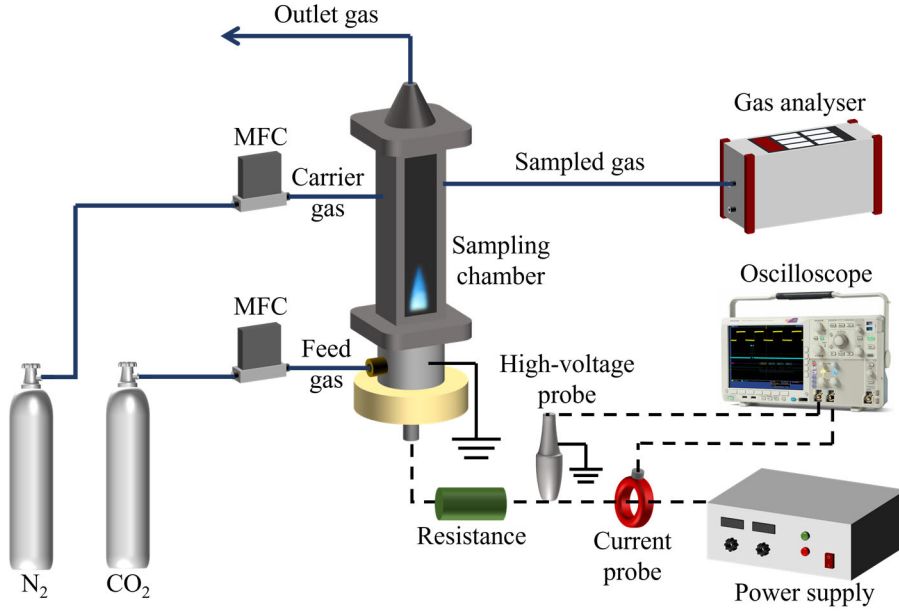


Fig. S1. Schematic of the experimental setup

The gas temperature in the sampling tube was estimated in the range of 400-600 K, based on the calculation given below:

We assumed that it was an isobaric adiabatic mixing process.

Gas flow rate: $m_c = 1.25 \text{ g/min}$, $m_s = 0.6 \text{ g/min}$

Gas temperature before mixing: $T_{1c} = 300 \text{ K}$, $T_{1s} = 500 \sim 1300 \text{ K}$

where m_c and m_s are the mass flow rates of carrier gas and sampled gas, respectively; T_{1c} and T_{1s} are the initial temperature of carrier gas and sampled gas, respectively.

Gas temperature after mixing:

$$T_2 = \frac{m_c \bar{c}_{p,c} T_{1c} + m_s \bar{c}_{p,s} T_{1s}}{m_c \bar{c}_{p,c} + m_s \bar{c}_{p,s}} \quad (S1)$$

where $\bar{c}_{p,c}$ and $\bar{c}_{p,s}$ are the average specific heat at constant pressure. Since they are very similar, we assume that they are equal here. Thus, $T_2 \approx 400 \sim 600 \text{ K}$.

S2 Model description

The model is calculated using COMSOL Multiphysics and is a fully coupled combination of calculating the gas velocity and pressure, temperature, species concentrations and how these species are distributed over the reactor.

S2.1 Gas flow

The laminar gas flow is calculated using the Navier-Stokes equations for conservation of mass and momentum in their time-dependent form:

$$\frac{\partial \rho}{\partial t} + \nabla \cdot (\rho \vec{u}) = 0 \quad (S2)$$

$$\rho \frac{\partial \vec{u}}{\partial t} + \rho (\vec{u} \cdot \nabla) \vec{u} = \nabla \cdot \left[-p \vec{I} + \mu (\nabla \vec{u} + (\nabla \vec{u})^T) - \frac{2}{3} \mu (\nabla \cdot \vec{u}) \vec{I} \right] \quad (S3)$$

With ρ the gas density, t the time, \vec{u} the gas velocity vector, p the pressure, \vec{I} the identity matrix, μ the dynamic viscosity, and superscript T stands for the transpose of the velocity vector gradient. These equations are solved to obtain the velocity and pressure as a function of time and position in the 3D and 2D axisymmetric geometry. The flow is considered weakly compressible, which means that the density only depends on temperature, but does not vary with pressure. For the 3D model, the gas flow is assumed to be compressible, in which the density depends on both temperature and pressure.

The boundary conditions are divided into the inlet, the outlet and the walls.

(a) Inlet

The boundary condition at the inlet is given by:

$$\vec{u} = \vec{u}_0 \quad (S4)$$

The velocity \vec{u}_0 set at the inlet is obtained from the 3D gas flow model. A cross-section plane is defined in the 3D model at the height at which the 2D axisymmetric model starts, i.e., at -15 mm. On this plane, different concentric circles are drawn, with varying radii that correspond to specific values of r , and therefore specific points along the inlet line, corresponding to a surface, in the 2D axisymmetric model. A schematic drawing of the cross-section surface, the concentric circles and the velocity components is given in Fig. S2. For every radius, i.e., for every point along the inlet line, the velocity is calculated as the average velocity over the complete circle. This velocity consists of three velocity components, an r -, ϕ - and z -component in cylindrical coordinates that are each calculated separately and imposed separately on the inlet boundary in the 2D axisymmetric model. Because the ϕ -component of the velocity is not equal to 0 m/s on this plane, the swirl in the flow is included in the 2D axisymmetric model. The three velocity components in cylindrical coordinates are obtained from the velocities in Cartesian coordinates in the 3D model using the following equations:

$$v_r = \frac{xv_x + yv_y}{\sqrt{x^2 + y^2}} \quad (S5)$$

$$v_\phi = -\sqrt{v_x^2 + v_y^2} \times \sin\left(\cos^{-1}\left(\frac{xv_x + yv_y}{\sqrt{x^2 + y^2}\sqrt{v_x^2 + v_y^2}}\right)\right) \quad (S6)$$

$$v_z = v_z \quad (S7)$$

With x , y and z the Cartesian coordinates in the 3D model of the points on the circle, and v_x , v_y and v_z the three velocity components in Cartesian coordinates in the same point.

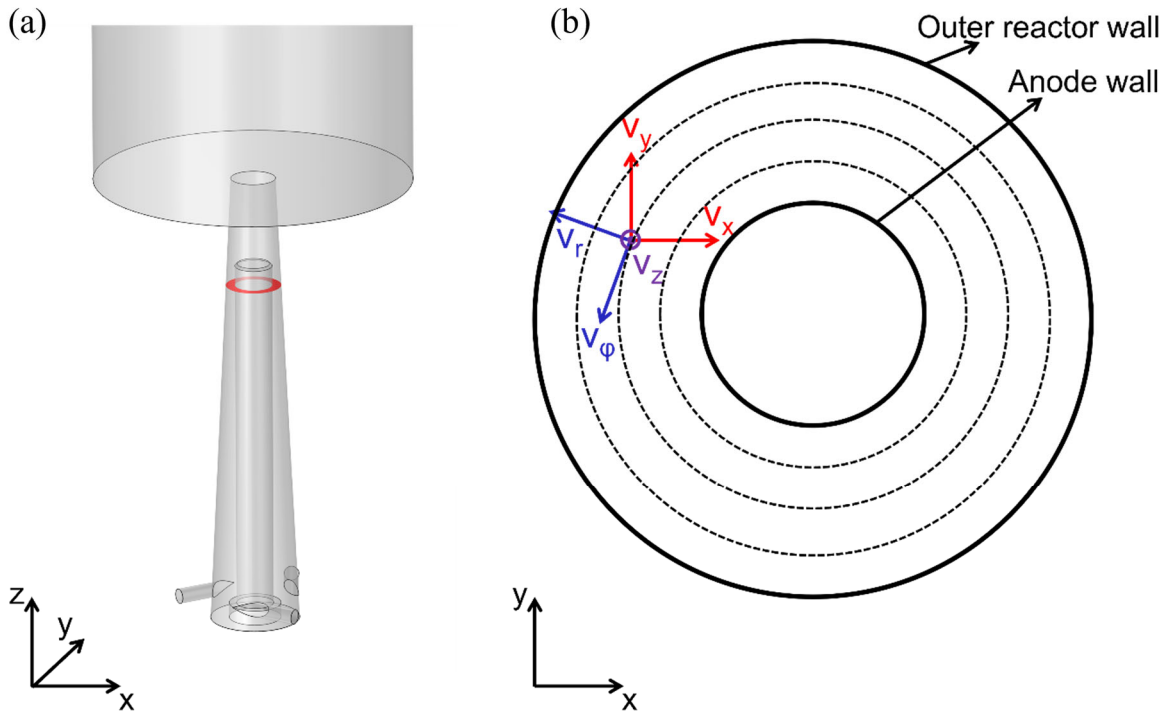


Fig. S2. (a) Drawing of the reactor part and start of the exhaust in the 3D model, indicating the ring-shaped cross-section surface at $z = -15$ mm (in red) that is used to obtain the velocity components for the 2D axisymmetric model, and (b) schematic drawing of the cross-section surface with the velocity components in Cartesian (in red) and cylindrical (in blue) coordinates indicated. The z -component of the velocity is pointing out of the page. The dashed concentric circles correspond to the different r -values at which the velocity components are calculated (more than the three circles shown here), as an average over one of these circles.

(b) Outlet

The outlet is defined as an open boundary and given by:

$$\left[-p\vec{I} + \mu(\nabla\vec{u} + (\nabla\vec{u})^T) - \frac{2}{3}\mu(\nabla \cdot \vec{u})\vec{I} \right] \vec{n} = \vec{0} \quad (S8)$$

With \vec{n} a unity vector normal to the outlet boundary and pointing out of the reactor.

(c) Walls

All walls have a no slip condition:

$$\vec{u} = \vec{0} \quad (S9)$$

S2.2 Heat transfer

The heat transfer module calculates the temperature through the heat balance equation:

$$\rho C_p \frac{\partial T}{\partial t} + \rho C_p \vec{u} \cdot \nabla T + \nabla \cdot \vec{q} = Q_p + Q_{vd} + Q_{heat\ source} + Q_{heat\ sink} \quad (S10)$$

$$\vec{q} = -k \nabla T \quad (S11)$$

$$Q_p = \alpha_p T \left(\frac{\partial p}{\partial t} + \vec{u} \cdot \nabla p \right) \quad (S12)$$

$$Q_{vd} = \tau : \nabla \vec{u} \quad (S13)$$

With C_p the specific heat capacity at constant pressure, T the temperature, \vec{q} the conductive heat flux, Q_p the heat corresponding to work resulting from pressure changes, Q_{vd} the heat due to viscous dissipation, while $Q_{heat\ source}$ and $Q_{heat\ sink}$ are the heat source and heat sink defined in our model, representing the plasma and accounting for cooling in the afterglow, respectively. Note that the heat sink has a negative value. The terms on the left-hand side in equation (S10) are the change in temperature over time, the convective and conductive heat transfer, respectively. Furthermore, in equations (S11-S13), k is the thermal conductivity, α_p the coefficient of thermal expansion, and τ the viscous stress tensor. The shape of the heat source and heat sink is indicated in Fig. 2 in the main paper, and the total power is then distributed over these shapes using two rectangle functions, in the r-direction and z-direction, with rounded edges; through the 2D axisymmetry of the model, together they create a cylindrical shape. Because the functions are rectangles, the powers are approximately equally distributed over the cylinders, except at the edges where there is a lower power distribution due to the rounding of these edges. Together, these equations provide the temperature as a function of time and position in the 2D axisymmetric geometry.

In the model, we use a heat sink to represent the effect of turbulent cooling. Indeed, we assume that the flow is laminar, to reduce complexity and computation time, but this means that turbulent heat transfer is not included. However, modelling of a gliding arc plasmatron reactor has revealed that turbulent heat transfer can become important, with a turbulent gas thermal conductivity about 100 times larger than the gas thermal conductivity without turbulence for an argon plasma [1]. In addition, it has also been demonstrated experimentally that the turbulence causes radial mixing after the plasma, by using Schlieren photographs [2]. The latter paper clearly shows the effect of plasma on the flow behaviour:

without plasma, the flow is laminar, but when a voltage is applied, the flow behaves turbulently and more mixing takes place, which can also happen in our setup but is not yet accounted for in the model.

This turbulence is caused by the movement of the arc. Based on the current-voltage curves and a video of the plasma measured during the experiment, we know that the arc is in so-called restrike mode. In this mode, reattachment of the arc takes place, which influences the flow significantly [3]. In this way, the distribution of heat, and therefore temperature, and particles will also be changed to some extent. However, modelling this restrike phenomenon requires more complicated models, including a more elaborate description of the (boundary layer of the) anode and a 3D geometry [3]. This would lead to excessive computation times, in combination with the calculation of the chemistry and particle transport, keeping in mind also the size of this reactor. Therefore, we use the above-described heat sink, to mimic the effect of turbulence and reattachment on the gas temperature. Because this turbulence, and therefore cooling, increases with increasing flow rates, we used a somewhat higher power of the heat sink at 7 L/min (i.e., 185 W) compared to 160 W at 5 L/min.

There are more separate boundary conditions for the heat transfer compared to the gas flow.

(a) Inlet

The inlet boundary condition is given by:

$$T = T_0 = 300 \text{ K} \quad (S14)$$

The temperature at the inlet is set to a constant value of the 300K. This corresponds to CO₂ gas that flows into the reactor at room temperature.

(b) Outlet

The heat transfer at the outlet has the following boundary condition:

$$-\vec{n} \cdot \vec{q} = 0 \quad (S15)$$

This means that there is no conductive heat flux through the outlet, both into and out of the reactor. As a consequence, heat inside the exhaust can only be transported out of the reactor outlet through convection, transported by the gas flow.

(c) Walls at the outside of the reactor and the start of the exhaust (orange in Fig. 2 of the main paper)

These walls are in contact with the air outside the reactor, and in close contact with the heat source, and are defined by a heat flux through the wall:

$$-\vec{n} \cdot \vec{q} = h(T_{ext} - T) \quad (S16)$$

The heat transfer by conduction for these walls is set to a certain value, calculated using the heat transfer coefficient h (in this case equal to 50 W/(m²K)), the external temperature of the air outside the reactor T_{ext} (here a constant value of 293.15 K), and the temperature at the wall inside the reactor T . When the

temperature T is higher than the external temperature, which is mostly the case, the heat conduction is directed outwards and the heat from the reactor is lost to the outside environment.

(d) *Cylinder side (brown in Fig. 2 of the main paper)*

The cylinder side has the same boundary condition as the inlet, namely:

$$T = T_0 = 300 \text{ K} \quad (S17)$$

Because there is no gas flow into or out of this wall, this boundary condition here means that the gas temperature close to the wall is set to 300 K.

(e) *Anode walls and walls at the end of the exhaust (pink and purple, respectively, in Fig. 2 of the main paper):*

These two separate groups of boundaries have the same thermal insulation boundary condition:

$$-\vec{n} \cdot \vec{q} = 0 \quad (S18)$$

This equation indicates that there is no conduction through these walls. The anode walls are, similar to the walls at the outside of the reactor, close to the heat source and in contact with high temperature gas. However, these walls are not directly connected to the room temperature gas surrounding the reactor. Therefore, they are given a thermal insulation boundary condition instead of a heat flux boundary condition.

S2.3 Chemistry and transport of chemical species

Modelling chemical transport includes both the reactions taking place inside the reactor, as well as the transport of the different species through the reactor. The transport equation for the different species, taking into account the conservation of mass, is based on the following equation:

$$\rho \frac{\partial \omega_i}{\partial t} + \nabla \cdot \vec{J}_i + \rho(\vec{u} \cdot \nabla) \omega_i = R_i \quad (S19)$$

With ω_i the mass fraction of species i , \vec{J}_i the mass flux of species i relative to the mass-averaged velocity and R_i the total net rate of production and destruction of species i . The terms on the left-hand side represent the change in mass fraction of species i over time, the diffusion of species i and its transport due to the gas flow, respectively, while the right-hand side corresponds to the change in species i due to reactions taking place in the reactor. This equation is used for four species included in the model, CO, O, O₂ and C, and these four equations are solved together to calculate their mass fractions, as a function of time and position in the 2D axisymmetric geometry. The mass fraction of CO₂ is obtained from the assumption that the sum of all mass fractions is equal to 1.

The mass flux \vec{J}_i used in the mass transport equation corresponds to molecular diffusion and is calculated as:

$$\vec{J}_i = -\left(\rho D_i^m \nabla \omega_i + \rho \omega_i D_i^m \frac{\nabla M_n}{M_n} - \rho \omega_i \sum_{i=1}^N \frac{M_i}{M_n} D_i^m \nabla x_i\right) \quad (S20)$$

$$D_i^m = \frac{1 - \omega_i}{\sum_{k \neq i}^N \frac{x_k}{D_{ik}}} \quad (S21)$$

$$M_n = \left(\sum_{i=1}^N \frac{\omega_i}{M_i}\right)^{-1} \quad (S22)$$

$$D_{ik} = 2.662821 \cdot 10^{-22} \frac{\sqrt{T^3 \frac{(M_i + M_k)}{(2 \cdot 10^3 M_i M_k)}}}{p \sigma_i \sigma_k \Omega_{D,diff}} \quad (S23)$$

$$\Omega_{D,diff} = \frac{c_1}{(T^*)^{c_2}} + \frac{c_3}{e^{c_4 T^*}} + \frac{c_5}{e^{c_6 T^*}} + \frac{c_7}{e^{c_8 T^*}} \quad (S24)$$

$$T^* = T \frac{k_B}{\sqrt{\varepsilon_i \varepsilon_k}} \quad (S25)$$

With D_i^m the mixture-averaged diffusion coefficient of species i , M_n the mean molar mass, M_i and M_k the molar mass of species i and k , respectively, x_i the mole fraction of species i , D_{ik} the multicomponent Maxwell-Stefan diffusivities for species i and k , σ_i and σ_k the potential characteristic length value of species i and k , and $\Omega_{D,diff}$ a collision integral used to calculate diffusion coefficients. c_1 to c_8 are eight empirical constants, k_B is the Boltzmann constant and ε_i and ε_k the potential energy minimum of species i and k . The potential characteristic lengths and potential energy minima are obtained from GRI-Mech 3.0 [4]. The sum is taken over all N species in equations (S20) and (S22), and over all species k , except i itself, in equation (S21). In this model, a mixture-averaged diffusion model is applied, which uses a Fick's law type approximation. In this approximation, the net diffusive mass flux is not equal to 0, which is why a correction term is added. This is the last term on the right-hand side of equation (S20).

The total net rate of production and destruction of species i , R_i in equation (S19), is calculated with the formula:

$$R_i = \sum_{j=1}^M \nu_{ij} r_j \quad (S26)$$

where r_j is the net rate of reaction j , calculated as:

$$r_j = k_j^f \prod_{i \in react} c_i^{-\nu_{ij}} - k_j^r \prod_{i \in prod} c_i^{\nu_{ij}} \quad (S27)$$

In these equations, ν_{ij} is the stoichiometric coefficient of species i in reaction j , the sum is taken over all M reactions, k_j^f and k_j^r are the forward and reverse rate coefficients of reaction j , respectively, c_i is

the molar concentration of species i , and the equation is split in terms calculating the forward reaction rate when i is a reactant and a reverse rate when i is a product.

The equations of the forward rate coefficients are given in Table 1 in the main paper. The reverse rate coefficients are calculated through detailed balancing, using the following equations [5]:

$$k_j^r = \frac{k_j^f}{K_j} \quad (S28)$$

$$K_j = e^{\left(\frac{\Delta S_j^0}{R} - \frac{\Delta H_j^0}{RT}\right)} \left(\frac{P_{atm}}{RT}\right)^{\sum_{i=1}^N \nu_{ij}} \quad (S29)$$

$$\Delta S_j^0 = \sum_{i=1}^N \nu_{ij} S_i^0 \quad (S30)$$

$$\Delta H_j^0 = \sum_{i=1}^N \nu_{ij} H_i^0 \quad (S31)$$

With K_j the equilibrium constant of reaction j , ΔS_j^0 and ΔH_j^0 the standard-state molar entropy and enthalpy of reaction j , respectively, R the gas constant, P_{atm} atmospheric pressure (101325 Pa), and S_i^0 and H_i^0 the standard-state molar entropy and enthalpy of species i , which are calculated using NASA polynomials [6]. The sum in these equations is calculated over all N species i in reaction j .

The changing composition of the gas influences the properties of this gas. The density is calculated using the ideal gas law, while the other gas properties are calculated using the following formulas.

(i) Heat capacity C_p :

$$C_p = \sum_{i=1}^N \omega_i \frac{C_{p,i}}{M_i} \quad (S32)$$

With $C_{p,i}$ the heat capacity at constant pressure for species i , which is obtained using NASA polynomials [6], and the other parameters are defined in earlier equations.

(ii) Dynamic viscosity μ :

$$\mu = \sum_{i=1}^N \frac{\mu_i}{1 + \frac{1}{x_i} \sum_{k \neq i}^N x_k \phi_{ik}} \quad (S33)$$

$$\phi_{ik} = \frac{\left[1 + \left(\frac{\mu_i}{\mu_k}\right)^{0.5} \left(\frac{M_k}{M_i}\right)^{0.25}\right]^2}{2\sqrt{2} \left[1 + \frac{M_i}{M_k}\right]^{0.5}} \quad (S34)$$

$$\mu_i = 2.669 \cdot 10^{-6} \frac{\sqrt{T M_i \cdot 10^3}}{\sigma_i^2 \Omega_{D,visc}} \quad (S35)$$

$$\Omega_{D,visc} = \frac{b_1}{(T^*)^{b_2}} + \frac{b_3}{e^{b_4 T^*}} + \frac{b_5}{e^{b_6 T^*}} + \frac{4.998 \cdot 10^{-40} \mu_{D,i}^4}{k_B^2 T \left(\frac{\varepsilon_i}{k_B}\right) \sigma_i^6} \quad (S36)$$

$$T^* = T \frac{k_B}{\varepsilon_i} \quad (S37)$$

Where μ_i and μ_k are the dynamic viscosity of species i and k , and $\Omega_{D,visc}$ another, dimensionless collision integral used to calculate the viscosity and thermal conductivity, b_1 to b_6 are empirical constants and $\mu_{D,i}$ is the dipole moment of species i , also obtained from GRI-Mech 3.0 [4]. More information on the two collision integrals $\Omega_{D,diff}$ (equation (S24)) and $\Omega_{D,visc}$ (equation (S36)) can be found in references 4 and 5. The sum in equation (S33) is taken over all N species at the start of the right-hand side and all N species, except species i itself, in the denominator.

(iii) *Thermal conductivity k :*

$$k = \frac{1}{2} \left(\sum_{i=1}^N x_i k_i + \frac{1}{\sum_{i=1}^N \frac{x_i}{k_i}} \right) \quad (S38)$$

$$k_i = \mu_i \cdot \frac{1.15 C_{p,i} + 0.88 R}{M_i} \quad (S39)$$

With x_i the mole fraction of species i , k_i the thermal conductivity of this species, μ_i the viscosity of species i , defined above in equation (S35) and $C_{p,i}$ the heat capacity at constant pressure of i .

The boundary conditions for the chemical transport are as follows:

(a) *Inlet*

The boundary condition at the inlet is given by:

$$\omega_i = \frac{x_{0,i} M_i}{M_n} \quad (S40)$$

with $x_{0,i}$ the mole fraction of every species i at the inlet, and the other parameters defined above. The inlet has a set mole fraction, converted to mass fraction, for all five species. For CO, O₂, O and C, these initial mole fractions are equal to 10^{-8} , which means that the mole fraction of CO₂ is equal to $1 - 4 \times 10^{-8}$. This value of 10^{-8} is chosen instead of 0 for numerical reasons, to let the simulation calculate more smoothly.

(b) *Outlet*

The mass transport at the outlet is defined as:

$$-\vec{n} \cdot \rho D_i^m \nabla \omega_i = 0 \quad (S41)$$

This means that there is no mass diffusion of any species i possible through the outlet, and species can only be removed from the reactor by the gas flow. This is similar to the outlet boundary condition for heat transfer, where only convection by the gas flow can transport heat from the reactor, but not conduction.

(c) Walls

All walls have a no flux boundary condition:

$$-\vec{n} \cdot \vec{j}_i = 0 \quad (S42)$$

This simply means that there is no mass transfer through the walls.

S3 Detailed calculation results

S3.1 Gas flow pattern in the reactor and exhaust

As can be seen from Fig. S3, the gas flows upwards in the centre of the reactor, coming directly from the inlet, and also flows upwards close to the walls. In between those two upward gas streams, there is a downwards flow. The latter is caused by the converging end of the reactor, close to the outlet. Part of the gas collides with this converging wall and recirculates back in the exhaust, taking the heat and higher concentration in CO and O₂ with it, and spreading it over the exhaust, away from the symmetry axis.

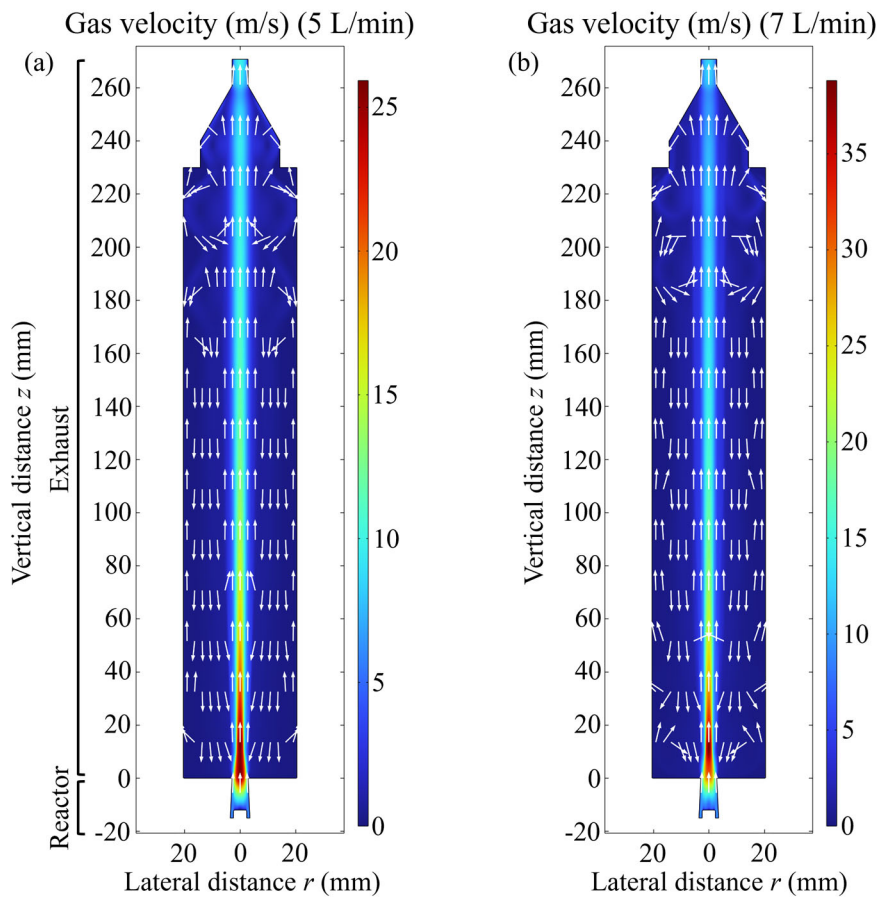


Fig. S3. Total flow velocity in the reactor and exhaust for (a) 5 L/min and (b) 7 L/min. The arrows indicate the direction of the flow in the points at the tails of the arrows.

S3.2 Reaction analysis

Figs. S4 and S5 present the reaction rates of the two CO_2 conversion reactions, and their splitting and recombination components for 7 L/min, similar to Figs. 5 and 6 for 5 L/min in the main paper. The plots look very similar to the results at 5 L/min, but with two larger differences. Firstly, the reaction rates, especially the recombination rate of reaction 1, are slightly more spread out to higher z -values in the afterglow for the higher flow rate of 7 L/min, which is a logical consequence of the increased convective heat transport in the axial direction, transporting the heat to higher positions in the reactor, although this difference is not always very clear. Secondly, the high temperature, and therefore the reaction rates, seem to be less attached to the anode at 7 L/min, which is also caused by the gas flow itself.

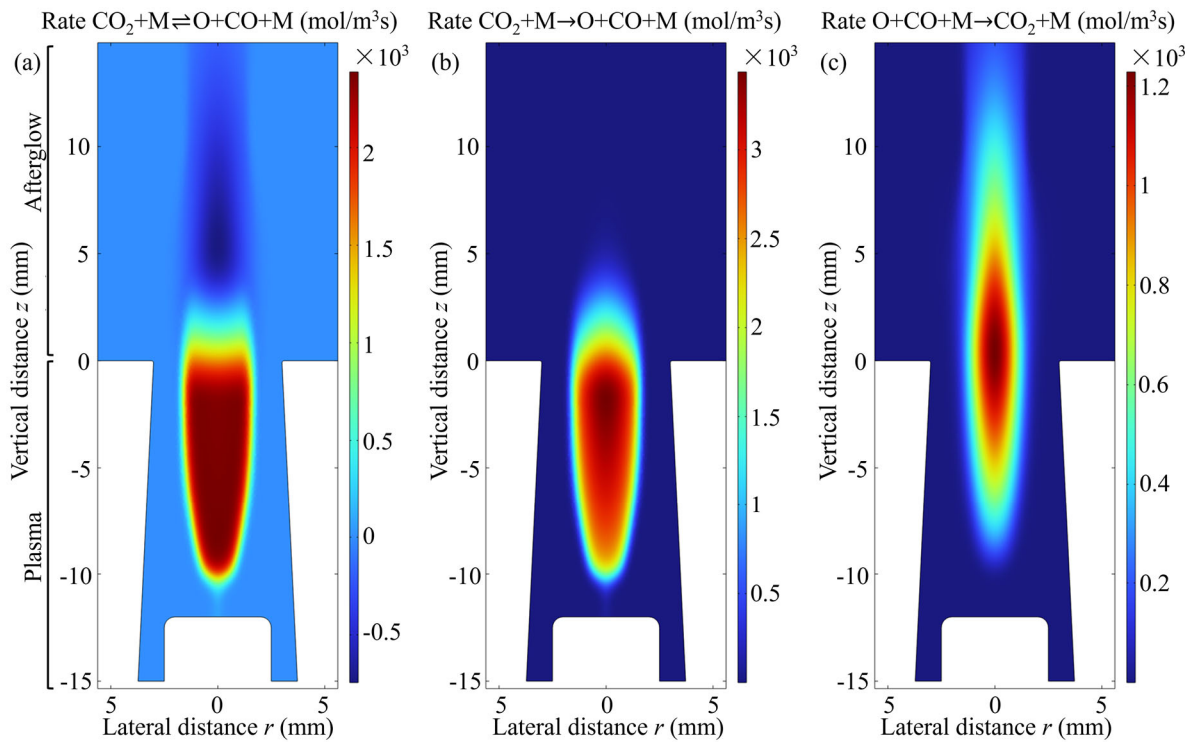


Fig. S4. Net rate of CO_2 conversion by the reaction $\text{CO}_2 + \text{M} \rightleftharpoons \text{O} + \text{CO} + \text{M}$ (a), and its breakdown into the splitting rate (forward reaction) (b) and the recombination rate (backward reaction) (c), at 7 L/min. The plasma is located at $z < 0$ mm, and the afterglow starts when the gas leaves the reactor and enters the exhaust at $z > 0$ mm.

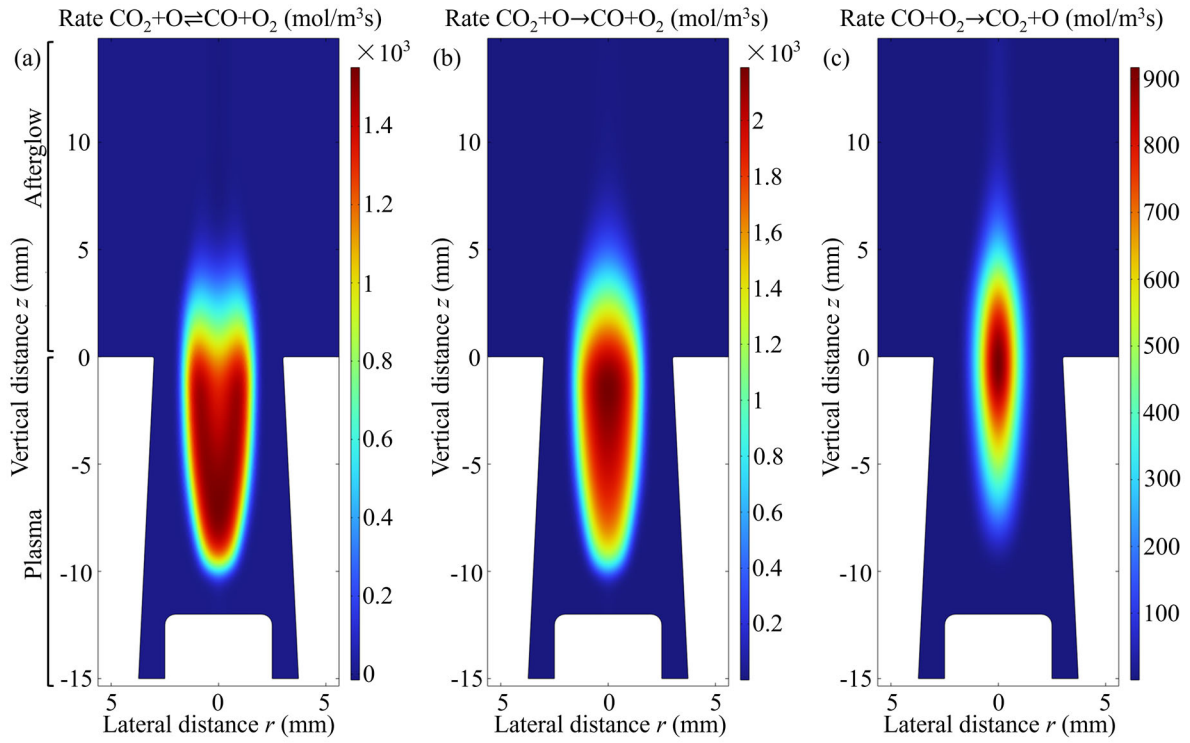


Fig. S5. Net rate of CO_2 conversion by the reaction $\text{CO}_2 + \text{O} \rightleftharpoons \text{CO} + \text{O}_2$ (a), and its breakdown into the splitting rate (forward reaction) (b) and the recombination rate (backward reaction) (c), at 7 L/min. The plasma is located at $z < 0$ mm, and the afterglow starts when the gas leaves the reactor and enters the exhaust at $z > 0$ mm.

Fig. S6 illustrates the concentration of O atoms in the reactor and the start of the exhaust. The O atom concentration remains relatively high in the first few millimetres of the exhaust and only drops below 1 % of its maximum value along the central axis at 22.2 mm and 33.1 mm (not visible in the plots), for 5 and 7 L/min, respectively.

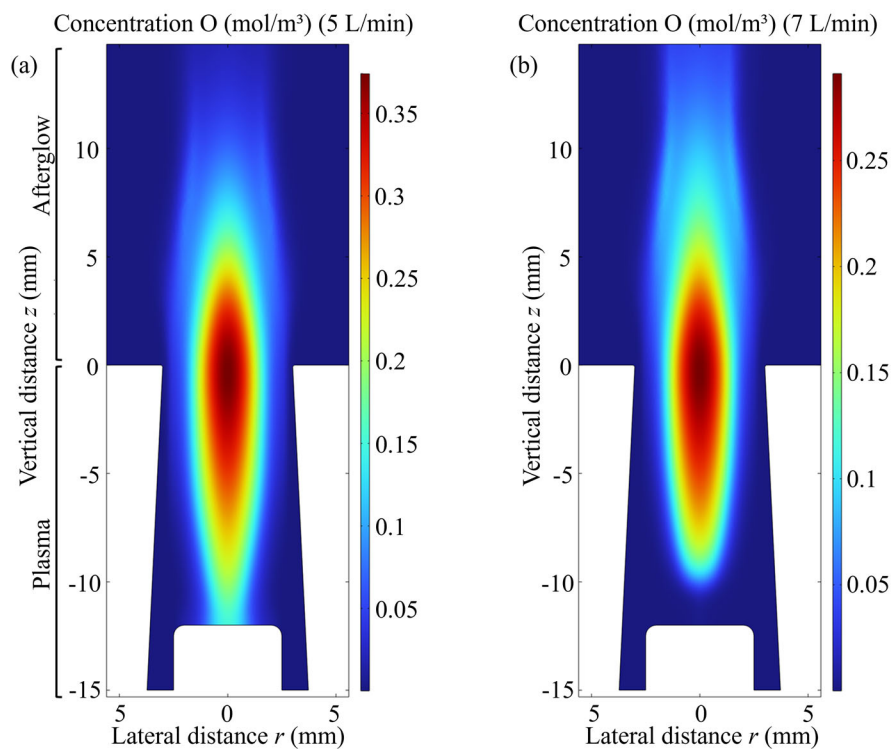


Fig. S6. Concentration of O atoms in the reactor and the start of the exhaust for 5 L/min (a) and 7 L/min (b).

S4 Afterglow quenching

The relative improvements of CO₂ conversion in Fig. 10 were calculated as below:

$$\text{Relative improvement (as factor)} = \frac{X_{CO_2}^{UC}(\%) - X_{CO_2}^{\frac{W}{OC}}(\%)}{X_{CO_2}^{\frac{W}{OC}}(\%)} \quad (S43)$$

where $X_{CO_2}^{UC}$ is the CO₂ conversion with solely upstream cooling, but the same formula applies for the CO₂ conversion with solely downstream cooling ($X_{CO_2}^{DC}$) or with both cooling ($X_{CO_2}^{UC+DC}$); $X_{CO_2}^{W/OC}$ is the CO₂ conversion without cooling. The relative improvements of energy efficiency were calculated in the same way; just replacing X with η .

The proportion of input energy used for gas heating was estimated by calculating the energy required to heat the inlet gas (pure CO₂) to 1200°C, assuming this heating process is carried out at constant pressure. It should be noted that the calculated values here are only estimates.

Discharge power: 480W

Inlet flow rate Q_{in} : $Q_{in} = 6 \text{ L/min}$ (273 K, 101325 Pa)

Inlet temperature T_1 : $T_1 = 20^\circ\text{C}$, outlet temperature T_2 : $T_2 = 1200^\circ\text{C}$

Inlet mass flow rate M_{in} :

$$M_{in}(g/s) = \frac{Q_{in}(L/min) \times 1.977(g/L)}{60(s/min)} = 0.1977(g/s) \quad (S44)$$

Gas heat absorption power q :

$$q(W) = M_{in}(g/s) \times (\bar{c}_{p_0}^{T_2}(J/(g \cdot K)) \times T_2(^{\circ}\text{C}) - \bar{c}_{p_0}^{T_1}(J/(g \cdot K)) \times T_1(^{\circ}\text{C})) = 270 \text{ W} \quad (S45)$$

where $\bar{c}_{p_0}^T$ is the average specific heat at constant pressure for the gas as it is heated from 0°C to temperature t (°C). $\bar{c}_{p_0}^{20} = 0.825 \text{ J/(g} \cdot \text{K)}$, $\bar{c}_{p_0}^{1200} = 1.153 \text{ J/(g} \cdot \text{K)}$

Thus, about 56% of input energy is used for gas heating.

References

- [1] G. Trenchev, S. Kolev, W. Wang, M. Ramakers, A. Bogaerts, CO₂ Conversion in a Gliding Arc Plasmatron: Multidimensional Modeling for Improved Efficiency, *J. Phys. Chem. C.* 121 (2017) 24470-24479. <http://doi.org/10.1021/acs.jpcc.7b08511>.
- [2] F. Liu, B. Zhang, Z. Fang, M. Wan, H. Wan, K.K. Ostrikov, Jet-to-jet interactions in atmospheric-pressure plasma jet arrays for surface processing, *Plasma Process. Polym.* 15 (2018). <http://doi.org/10.1002/ppap.201700114>.
- [3] J.P. Trelles, C. Chazelas, A. Vardelle, J.V.R. Heberlein, Arc Plasma Torch Modeling, *J. Therm. Spray Technol.* 18 (2009) 728-752. <http://doi.org/10.1007/s11666-009-9342-1>.
- [4] G.P. Smith, D.M. Golden, M. Fenklach, N.W. Moriarty, B. Eiteneer, M. Goldenberg, C.T. Bowman, R.K. Hanson, S. Song, W.C. Gardiner Jr., V.V. Lissianski, Z. Qin, GRI-Mech 3.0, <http://combustion.berkeley.edu/gri-mech/version30/text30.html>.
- [5] Reaction Design. ANSYS Chemkin Theory Manual 17.0 (15151), San Diego, 2015.
- [6] B. McBride, M. Zehe, S. Gordon, NASA Glenn Coefficients for Calculating Thermodynamic Properties of Individual Species, 2002.